

CASPER

Coupled Air–Sea Processes and Electromagnetic Ducting Research

QING WANG, DENNY P. ALAPPATTU, STEPHANIE BILLINGSLEY, BYRON BLOMQUIST, ROBERT J. BURKHOLDER,
ADAM J. CHRISTMAN, EDWARD D. CREEGAN, TONY DE PAOLO, DANIEL P. ELEUTERIO,
HARINDRA JOSEPH S. FERNANDO, KYLE B. FRANKLIN, ANDREY A. GRACHEV, TRACY HAACK,
THOMAS R. HANLEY, CHRISTOPHER M. HOCUT, TEDDY R. HOLT, KATE HORGAN, HAFLIDI H. JONSSON,
ROBERT A. HALE, JOHN A. KALOGIROS, DJAMAL KHELIF, LAURA S. LEO, RICHARD J. LIND, IOSSIF LOZOVATSKY,
JESUS PLANELLA-MORATO, SWAGATO MUKHERJEE, WENDELL A. NUSS, JONATHAN POZDERAC,
L. TED ROGERS, IVAN SAVELYEV, DANA K. SAVIDGE, R. KIPP SHEARMAN, LIAN SHEN, ERIC TERRILL,
A. MARCELA ULATE, QI WANG, R. TRAVIS WENDT, RUSSELL WISS, ROY K. WOODS, LUYAO XU,
RYAN T. YAMAGUCHI, AND CAGLAR YARDIM

The objective of CASPER is to improve our capability to characterize the propagation of radio frequency (RF) signals through the marine atmosphere with coordinated efforts in data collection, data analyses, and modeling of the air–sea interaction processes, refractive environment, and RF propagation.

ATMOSPHERIC VERTICAL STRUCTURE AND EM DUCTING. Propagation of electromagnetic (EM) waves from radar or communication devices can be significantly impacted by atmospheric refractive conditions associated with the vertical thermodynamic structure of the atmospheric boundary layer (e.g., Tatarski 1961; Turton et al. 1988). This article describes a coordinated effort to quantify atmospheric effects on EM propagation in the marine atmospheric boundary layer (MABL) via a multidisciplinary project called the Coupled Air–Sea Processes and Electromagnetic Ducting Research (CASPER).

Characteristics of radio frequency (RF) propagation in the atmosphere are identified through the index of refraction n or, more commonly, refractivity N , defined as $N = (n - 1) \times 10^6$. While there are methods for measuring N directly (e.g., refractometers), it

is often easier to estimate refractivity from measured atmospheric thermodynamic properties using

$$N = \frac{77.6}{T} \left(p + 4810 \frac{e}{T} \right), \quad (1)$$

where T is air temperature (K), p is atmospheric pressure (hPa), and e is water vapor pressure (hPa) (Battan 1973). Considering the curvature of the Earth, the modified refractivity M characterizes the radar propagation more directly:

$$M = N + \frac{z}{R} \times 10^6, \quad (2)$$

where z is the height above the surface and R is the mean radius of the Earth (Bean and Dutton 1968). Various propagation conditions can be defined by the vertical gradients of M , resulting in three anomalous propagation (AP) conditions: subrefraction,

superrefraction, and ducting. The latter is the most studied AP condition, as it represents sufficient bending of the ray toward the surface such that it becomes trapped within a duct, a channel where the EM energy is confined and propagates to extended ranges (Turton et al. 1988). Figure 1 illustrates the propagation path, indicated by the gray lines over the curved Earth surface, in three types of ducts. The trapping layers and the resultant duct layers in each ducting condition are defined by the M profiles and particularly their vertical gradients. The trapping layer is the layer with $dM/dz < 0$, resulting in downward bending of radio waves with a curvature smaller than that of the surface of the Earth. A trapping layer starting at the surface results in a surface duct in which RF energy is trapped between the surface and the top of the trapping layer (Fig. 1a). Hence, the trapping layer is also the duct layer. A subset of surface ducts are evaporation ducts that are prevalent over water (Brooks et al. 1999). An elevated trapping layer can result in either an elevated duct or a surface-based duct depending on the M profiles. If the M value at the surface is higher than that of the trapping-layer top (Fig. 1b), the duct is referred to as a surface-based duct. Otherwise, it is an elevated duct (Fig. 1c). In both surface and surface-based ducts, the propagation of the waves is also affected by the reflection and diffraction of the underlying surface as depicted in Figs. 1a and 1b. In the case of the elevated duct, the base of the duct is the altitude where the M value is the same as that at the trapping-layer top (Fig. 1c).

It is worth noting, though, that ducts are not bounded by impenetrable boundaries (except for the surface of the Earth) and RF energy is continually “leaked” outside the ducts at reduced intensity. A region of reduced RF energy above the duct is

referred to as a “radar hole” because of insufficient energy for radar detection. In addition, the geometry of the duct and trapping layers and the strength of the duct, often defined as the M difference of the trapping layer, are critical properties of a duct that regulate the impact of the duct on EM propagation. These properties of the duct, together with the M profile itself, determine the effects of the duct on the EM waves going through the medium. An intensity of the duct can be also defined relating these quantities to the maximum wavelength or the minimum frequency of the RF signal to be impacted by the duct (Kerr 1951; Turton et al. 1988).

Analyses of the gradient of M expressed in Eq. (2) reveal the vertical gradient of water vapor pressure as the dominant term in dM/dz followed by the temperature gradient. As such, a hydrolapse and/or a temperature inversion both lead to a trapping layer. Any atmospheric processes resulting in a hydrolapse and/or a temperature inversion hence often result in ducting. Processes leading to ducting include ocean surface evaporation (hydrolapse), large-scale or frontal subsidence (elevated dry inversion), warm- and dry-air advection, and nocturnal radiative cooling over land. Of most interest to CASPER is a special type of surface duct: the evaporation duct (ED), which is almost always present over the oceans (Babin et al. 1997). Evaporation ducts result from a large humidity gradient immediately above the sea surface (see Fig. 1a). They are typically on the order of a few meters to a few tens of meters deep. The evaporation duct height (EDH) is dependent on atmospheric surface layer characteristics and is a major input to microwave propagation prediction models (Babin et al. 1997). Konstanzer (1994) showed that EDH should have an accuracy of better than 2 m in order

AFFILIATIONS: QING WANG, FRANKLIN, JONSSON, HALE, LIND, NUSS, ULATE, WENDT, WOODS, AND YAMAGUCHI—Naval Postgraduate School, Monterey, California; ALAPPATTU—Naval Postgraduate School, Monterey, and Moss Landing Marine Laboratories, Moss Landing, California; BILLINGSLEY, HORGAN, AND WISS—Naval Surface Warfare Center Dahlgren Division, Dahlgren, Virginia; BLOMQUIST AND GRACHEV—University of Colorado Boulder, and NOAA/ESRL, Boulder, Colorado; BURKHOLDER, MUKHERJEE, POZDERAC, QI WANG, XU, AND YARDIM—The Ohio State University, Columbus, Ohio; CHRISTMAN, FERNANDO, LEO, LOZOVATSKY, AND PLANELLA-MORATO—University of Notre Dame, Notre Dame, Indiana; CREGAN AND HOCUT—U.S. Army Research Laboratory, Adelphi, Maryland; DE PAOLO AND TERRILL—Scripps Institution of Oceanography, University of California, San Diego, La Jolla, California; ELEUTERIO—Office of Naval Research, Arlington, Virginia; HAACK AND HOLT—U.S. Naval Research Laboratory, Monterey, California; HANLEY—Applied Physics Laboratory, Johns

Hopkins University, Laurel, Maryland; KALOGIROS—National Observatory of Athens, Athens, Greece; KHELIF—University of California, Irvine, Irvine, California; ROGERS—Space and Naval Warfare Systems Center, San Diego, California; SAVELYEV—Remote Sensing Division, Naval Research Laboratory, Washington, D.C.; SAVIDGE—Skidaway Institute of Oceanography, University of Georgia, Savannah, Georgia; SHEARMAN—Oregon State University, Corvallis, Oregon; SHEN—University of Minnesota, Twin Cities, Minneapolis, Minnesota
CORRESPONDING AUTHOR: Qing Wang, qwang@nps.edu

The abstract for this article can be found in this issue, following the table of contents.

DOI:10.1175/BAMS-D-16-0046.1

In final form 28 September 2017

©2018 American Meteorological Society

For information regarding reuse of this content and general copyright information, consult the [AMS Copyright Policy](#).

to avoid significant errors in propagation prediction.

Many ED models are based on Monin–Obukhov similarity theory (MOST) in various forms. Earlier ED models of Jeske (1971, 1973), Paulus (1984, 1985), and Musson-Genon et al. (1992) used the original MOST empirical functions of Businger et al. (1971). Since then, various adjustments to MOST coefficients have been made (Babin et al. 1997; Frederickson 2012). Better alternatives are not yet available and MOST-based ED models have some known potential issues. First of all, many of the empirical profiles were obtained from measurements over land, and their adequacy for the marine atmospheric surface layer (MASL) has not been thoroughly evaluated. Edson et al. (2004) and McGillis et al. (2004) made extensive near-surface profile measurements of scalars such as temperature, water

vapor, and carbon dioxide. They both suggested that MOST is valid within the MASL above the wave boundary layer. This is good news for some applications, although more measurements are needed to further evaluate MOST in the MASL. The second issue is the role of wave/swells in modifying the scalar profiles. There is growing evidence that a wave-driven surface layer invalidates MOST (e.g., Rutgersson et al. 2001), and the overall impact of swell throughout the MABL has been found to extend higher than the general notion that a wave boundary layer is shallower than ~3 m (e.g., Makin and Mastenbroek 1996; Sullivan et al. 2008). Many of the wave/swell boundary layer studies have focused on momentum transfer at the air–sea interface, and only a few have focused on temperature and humidity (Anderson et al. 2004; Smedman et al. 2007). Smedman et al. (2007) indicate that the MOST relationship for temperature breaks down in a regime

when the Obukhov length is less than –150 m, a possible result of breaking waves. These results point to a need to understand the wave boundary layer and how it affects the complete M profile of the MASL. Furthermore, MOST is based on the assumptions of horizontal homogeneity and stationarity; it is likely to fail in the presence of a heterogeneous boundary layer and time-dependent surface forcing at disparate horizontal scales (e.g., Mahrt and Khelif 2010; Mahrt et al. 2014). These scientific issues involved in quantifying evaporation ducts are the motivations behind the CASPER program.

CASPER OVERVIEW. The CASPER science objectives were developed based on findings from numerous previous studies, particularly field programs such as the Wallops-2000 Microwave Propagation Measurement Experiment (Stapleton et al. 2001; Thompson and Haack 2011) and the Rough

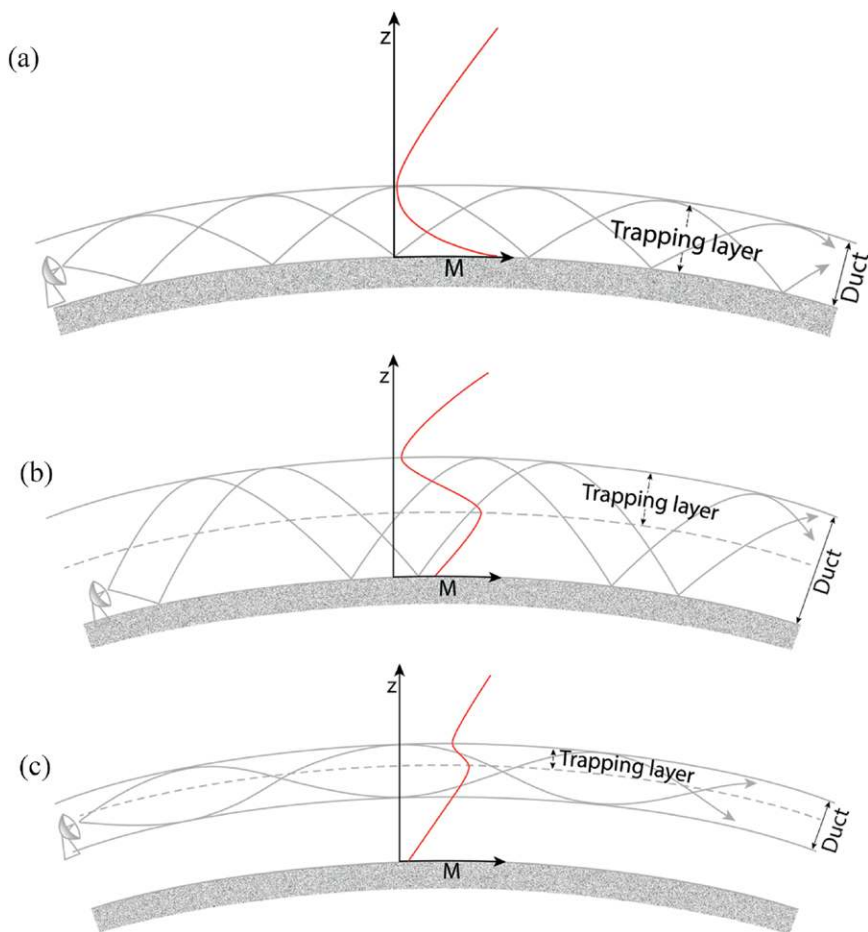


FIG. 1. Illustration of the propagation of EM waves from a radar source in various refractive conditions over a distance beyond line of sight over the Earth. The corresponding vertical profiles of the modified refractivity (M) are overlaid on the propagation path: (a) evaporation duct, (b) surface-based duct, and (c) elevated duct. [(Adapted from Turton et al. (1988).]

Evaporative Duct (RED) experiment (Anderson et al. 2004). The Wallops-2000 dataset has been a major source for many EM propagation modeling efforts in the past 15 years (e.g., Haack et al. 2010), largely due to the availability of range-dependent propagation measurements at multiple altitudes and concurrent meteorological measurements. A recent field campaign, the Tropical Air–Sea Propagation Study (TAPS), generated a unique dataset for clear-air tropical littoral conditions around Australia’s Great Barrier Reef that includes both extensive surface-layer turbulence and profile measurements and an RF dataset with multiple frequencies (Kulesa et al. 2017). With the significant improvements in atmospheric and EM propagation modeling in the past 20 years, there is, however, a general inadequacy of observational data available for model evaluation and further improvement. The CASPER objectives are as follows:

- to obtain a comprehensive and cohesive dataset to support in-depth analyses and modeling studies to address critical issues in air–sea interaction processes related to EM propagation;
- to improve MASL models in representing temperature and water vapor profiles in heterogeneous environments and under the effects of waves/swell;
- to understand physical processes governing the properties of the inversion layer atop the MABL and improve their representation in EM propagation models; and

- to explore new approaches in EM modeling to represent the impact of the atmospheric environment with spatial and temporal variability.

To achieve these objectives, CASPER assembled a multidisciplinary team to engage in intensive data collection field campaigns and extensive modeling efforts. Observations and model simulations were fully integrated through experiment design, data analyses, and model evaluation and improvement. CASPER environmental modeling efforts use a suite of advanced simulation tools, including large-eddy simulations (LESs) with a dynamically coupled atmospheric surface layer and phase-resolving wave field (Yang et al. 2013; Xie et al. 2016). The U.S. Navy’s Coupled Ocean–Atmosphere Mesoscale Prediction System (COAMPS; Doyle et al. 2012, 2014; Chen et al. 2010) was used in real time to support field measurement planning as well as mapping out spatial variability of refractive conditions.

CASPER includes two major field campaigns: the CASPER-East intensive observational period (IOP) conducted offshore of Duck, North Carolina (NC), 10 October–6 November 2015, and CASPER-West was conducted offshore of Pt. Mugu, California, from 27 September to 26 October 2017. The focus of CASPER-East was on assessing the effects of a heterogeneous marine environment on EM propagation and quantifying uncertainties in evaporation duct modeling. CASPER-West observations were designed

to evaluate wave/swell effects on evaporation duct properties and modeling issues associated with elevated trapping layers. Observations from these field campaigns should result in comprehensive datasets related to air–sea interaction processes using new measurement techniques and sampling strategies specifically targeting EM propagation. These field experiments were also designed to support CASPER modeling efforts for model initialization and validation to improve predictive capabilities for EM propagation. The success of the CASPER field campaigns entails synergistic collaborations

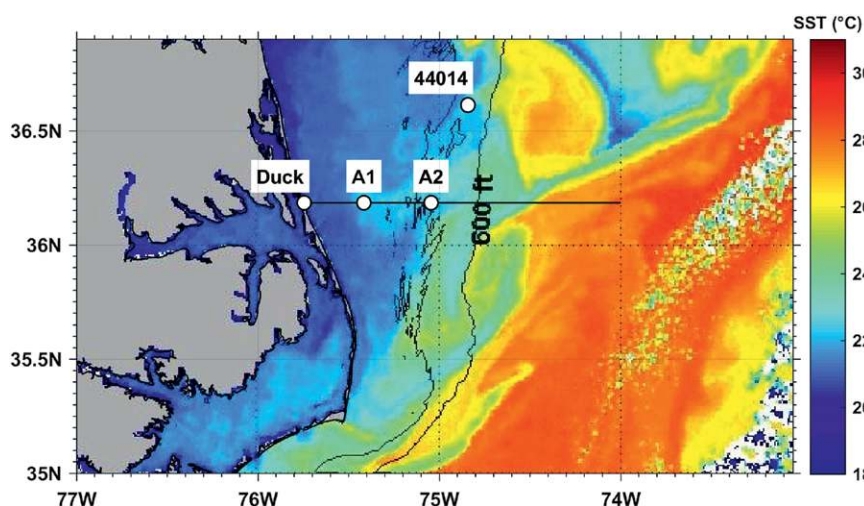


FIG. 2. SST measured from the NOAA-18 satellite on 16 Oct 2015. Location of offshore National Data Buoy Center buoy 44014 is noted together with the CASPER track from Duck pier toward the Gulf Stream. Points A1 and A2 are 16 (R16) and 34 (R34) n mi from Duck, NC, respectively, where moored floats were deployed at the beginning of the IOP. For a given day, one of the locations was used as the surface supersites with small buoys and balloons tethered to the predeployed floats.

across a diverse group of scientists and engineers specializing in MABL physics and modeling, upper-ocean and air–sea interaction processes, and RF propagation. The remainder of this article will focus on documenting various aspects of the first CASPER field campaign, CASPER-East.

CASPER-EAST FIELD CAMPAIGN. *SST variability in the CASPER-East IOP region.* CASPER-East occurred offshore of Duck, NC, and covered from the shelf region to the Gulf Stream (GS). This region is located at the southern end of the Mid-Atlantic Bight (MAB), the continental shelf between Nantucket Shoals and Cape Hatteras. The water near shore is generally cooler and lower in salinity than the oceanic waters seaward of the shelf, commonly termed the “slope water” (Shearman and Lentz 2010). The boundary between these two water masses occurs in a narrow transition region known as the shelf–slope front (Linder and Gawarkiewicz 1998). The northward-flowing GS is farther east, with strong currents and warm water that stimulate strong dynamic and thermodynamic responses on the continental shelf (Morgan and Bishop 1977; Lee et al. 1984). As a result, the region offshore of Duck, NC, displays strong local variabilities in temperature and salinity with mean water temperature and salinity increasing from nearshore toward the GS. Figure 2 shows sea surface temperature (SST) on 16 October 2015 from the NOAA-18 satellite. The general increase in SST and the mesoscale spatial variability are clearly

seen from Duck, NC, toward the GS. The black line in Fig. 2 is due east from Duck and is the path of all CASPER mobile platforms over the shelf region. This path is referred to as the CASPER track. During the CASPER-East field campaign, waypoints along the track were referenced as “Rxx,” where “xx” was the distance to shore in nautical miles.

The GS farther east is a region of significant air–sea coupling and heat transfer. The sharp SST front not only imparts abrupt changes in surface fluxes, thermal stability, low-level clouds, secondary circulation, and surface roughness (e.g., Sweet et al. 1981; Small et al. 2008) but also imposes anomalous radar propagation in the area (Glaeser 1978). Figure 3 illustrates the expected variations of SST, currents, surface waves, and mesoscale circulations associated with the land–sea temperature contrast and the GS SST front. Given the SST variabilities near the coast and at the GS SST front, internal boundary layer developments are likely across the SST gradient regions (Sweet et al. 1981). In general, the GS is 60–100 km from the shore. This is an ideal range for a midrange research aircraft, allowing sufficient on-station time for detailed sampling. Given the strong spatial and temporal variability of the lower atmosphere and the ocean, comprehensive sampling in both media is essential to understand the physical processes that contribute to the observed surface layer and EM propagation properties.

CASPER platforms, instruments, and instrument siting. CASPER emphasized concurrent environmental

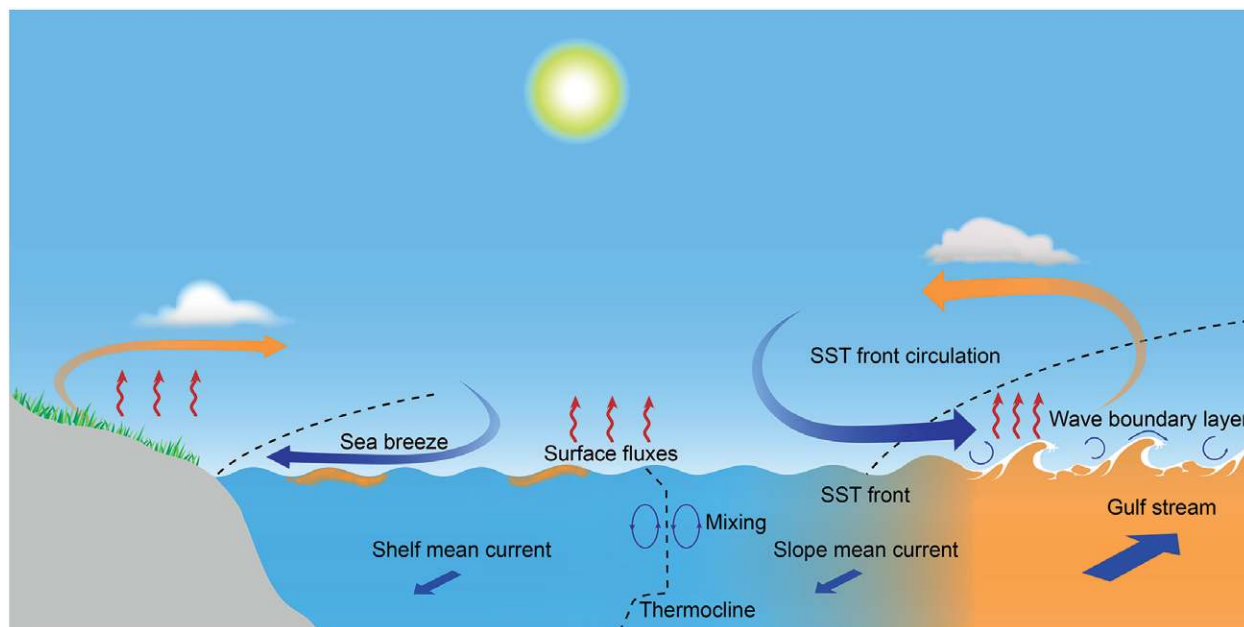


FIG. 3. Illustration of spatial variability of ocean currents, SSTs, surface waves, atmospheric mesoscale circulations, and internal boundary layer developments in the CASPER-East measurement region.

TABLE 1. Summary of CASPER-East observational assets.

Platform	Subject	Investigator(s)	Measurements
R/V <i>Sharp</i>	Atmosphere	Wang	Ship mean meteorology and turbulent fluxes from the bow mast, ocean skin temperature from infrared SST autonomous radiometer, cloud-base height, rawinsondes
R/V <i>Sharp</i>	RF propagation	Burkholder	EM emitters in X band
R/V <i>Sharp</i>	Surface waves	Terrill/de Paolo	WaMoS II wave field within 3 km of the ship
R/V <i>Sharp</i>	Upper-ocean physics	Shearman	Temperature and salinity profiles from bow chain
Work boat of R/V <i>Sharp</i>	MASL profiling	Wang	Tethered-balloon-based surface-layer profiling and near-surface mean p , T , and RH, water temperature
R/V <i>Atlantic Explorer</i>	Atmosphere	Fernando	Ship mean meteorology and turbulent fluxes from the bow mast, rawinsondes, scanning Doppler wind lidar, microwave radiometer, tethered-balloon low-level profiles of p , T , RH, and wind
R/V <i>Atlantic Explorer</i>	RF propagation	Burkholder, Yardim, Rogers	Four-level X-band receiving array, UWB receiving system, passive RF signal monitoring
R/V <i>Atlantic Explorer</i>	Upper-ocean physics	Shearman, Fernando, Lozovsky	Conductivity–temperature–depth (CTD) from bow chain, microstructure and turbulence dissipation from VMP, bow chain temperature and salinity profiles
CIRPAS Twin Otter	Atmosphere	Khelif, Wang	Mean state variables, turbulence, SST, radiation, aerosols, and clouds
CTV	Atmosphere	Khelif	Mean state variables, turbulence, SST, radiation
CTV	RF propagation	Burkholder	X-band beacon transmitter
R/V <i>Sharp</i> deployable surface platforms	Air–sea interaction	Wang	Surface Wave Glider, MASFlux, and tethered balloon on float for multilevel p , T , and RH, turbulence, ocean waves, and water temperature. All are part of the surface supersite.
Slocum Glider/microrider (4)	Upper-ocean physics	Shearman	CTD, turbulent kinetic energy dissipation, microstructure
Moored wave spectra buoy (5)	Ocean surface wave	Terrill/de Paolo	Wave spectra, water temperature
SAAB 340 aircraft	Upper-ocean turbulence	Savelyev	Aerial imaging of ocean surface temperature, waves, currents, and color
REMUS 100 AUV	Upper-ocean turbulence	Savelyev	CTD profiles and dye plume fluorimetry
Fishing boat “A-Salt Weapon”	Upper-ocean turbulence	Savelyev	Dye plume releases, REMUS 100 deployment and recovery, CTD casts
Bottom-mount VADCP and CT-Chain	Ocean	Savidge	Vertical velocity profiles, acoustic backscatter profiles, surface wave spectra, conductivity and temperature profile, at supersite A2 only
Duck shore site	Atmosphere	Fernando/Creegan, Horgan/Wiss, Wang, Hanley	Mean and flux tower at the end of Duck pier, onshore or on the sand dunes, scalar masts below pier deck, rawinsonde, scanning wind lidars
Duck shore site	RF propagation	Yardim, Horgan/Wiss	UWB and S, C, and X band transmitters

characterization, range-dependent EM propagation measurements, and extensive measurements on both sides of the air–sea interface. As such, multiplatform coordination was critical to achieve these measurement objectives. At the shore, the 550-m-long pier at Duck, NC, operated by the Field Research Facility (FRF) of the Coastal and Hydraulics

Laboratory of the U.S. Army Corps of Engineers (www.frf.usace.army.mil/) provided an ideal location that hosted an extensive suite of in situ and remote sensors. The moving platforms included two regional research vessels, R/V *Hugh R. Sharp* (hereafter *HRS*) and R/V *Atlantic Explorer* (hereafter *AE*), and a research aircraft, the Twin Otter (TO) and its



FIG. 4. Pictures of CASPER-East major platforms, surface sites, and towers.

Controlled Towed Vehicle (CTV) operated by the Center for Interdisciplinary Remote-Piloted Aircraft Studies (CIRPAS) at the Naval Postgraduate School (NPS). The TO and CTV provided high-resolution in situ measurements of temperature, humidity, SST, 3D winds, turbulent fluxes via the eddy correlation method, and their spatial variability required for RF propagation and ducting studies. The CTV is a tethered drone instrumented for atmospheric and ocean surface measurements similar to those on the TO. It was capable of maintaining radar altitude as low as 9 m above the ocean surface while towed from the TO at 300 m. This fast-moving platform sampled over a large area in a relatively short time period, resulting in a “snapshot” of the refractivity profiles along the path. Given the TO had a minimum altitude limit of 30 m MSL, the CTV provided direct measurements of mean and turbulent meteorological parameters and fluxes at the canonical 10-m height without invoking the assumptions of MOST (Kalogiros and Wang 2011). The TO/CTV aptly complemented measurements from the slow-moving and stationary platforms, buoys, piers, and shore towers. The

wide-area coverage provided extensive sampling of wind and SST heterogeneity and ducting conditions. In addition, as part of the collaborative efforts from the U.S. Naval Research Laboratory, a Saab 340 joined CASPER with remote sensing capabilities for ocean surface measurements. Table 1 lists specific measurements made from each platform/site and the responsible investigators. Pictures of major platforms are shown in Fig. 4, and instrument locations on the ships are shown in Fig. 5. A summary of shore site instruments is given in Table 2.

Experiment design and platform coordination. The sampling strategy of the CASPER-East IOP focused on characterizing EM propagation and atmospheric refractive properties as well as air–sea processes along the propagation path. An important sampling strategy was to make repeated measurements along the same path to obtain larger sample sizes and to avoid influences of different topography, coastline, water depth, or bathymetry. CASPER-East targeted the effects of boundary layer heterogeneity from two different perspectives. On the mesoscale, variability

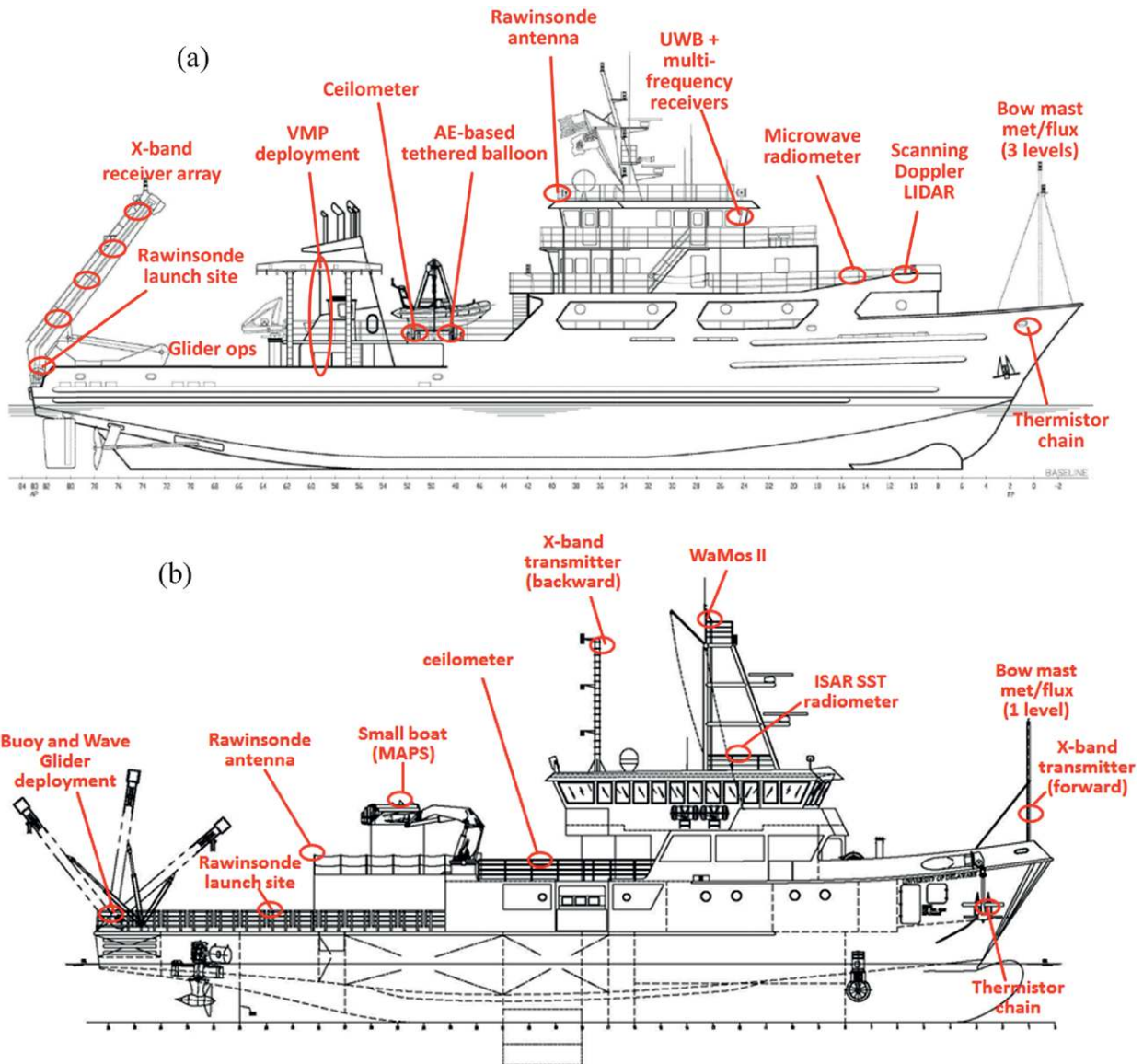


FIG. 5. CASPER-East instrument siting on (a) R/V *Atlantic Explorer* and (b) R/V *Hugh R. Sharp*.

of atmospheric refractivity requires range-dependent propagation measurements with corresponding characterization of environmental parameters. This requirement necessitated that the basic measurement strategy be mobile and able to sample along the propagation path. Second, the intention of CASPER-East was to collect extensive near-surface measurements for evaluation and improvement of ED models involving surface-layer similarity theory under heterogeneous conditions where MOST is likely to fail. Sampling away from the ships to avoid modification of surface air properties by the vessels was critical to the success of this effort. A cluster of small platforms, including moored small flux buoys [Marine Air–Sea Flux buoy (MASFlux)], an instrumented Wave Glider, a moored tethered balloon with

sensors at multiple levels, an underwater unmanned vehicle (UUV), and a mini wave buoy, were deployed in close proximity to each other at A1 (R16) or A2 (R34) in Fig. 2. These two locations were referred to as the surface supersites. Pictures of these small platforms are given in the bottom-left corner of Fig. 4. In addition, surface-layer flux from the ship bow masts and supporting profiling measurements from a small boat were made during dedicated periods referred to as the air–sea interaction (ASI) sampling module. For both ships, an ASI module includes turbulence measurements from bow masts with the bow facing the wind for 30–45 min and deployment of bow thermistor chains. During their respective ASIs, small-boat-based tethered balloon surface-layer profiling measurements were also made from *HRS*

TABLE 2. Instruments deployed from the pier or at the shore site at Duck, NC. Asterisks denote instruments deployed at a beachfront house 1.8 km north of the pier.		
Investigator	Short name	Description
Wang	2× scalar masts and radiation boom	North- and south-facing masts for <i>T</i> and RH at multiple levels below the pier deck plus one level of mean wind and 3D sonic turbulence
Jonsson	Navy aerosol sampling unit (NASU)	Passive cavity aerosol spectrometer probe, nephelometer, and soot-photometer for aerosol size distribution, scattering, and absorption
Fernando/ Creegan	50-ft tower, pier end	Three-level mean meteorology and 3D sonic turbulence, one-level LI-COR H ₂ O (50 ft = 15.24 m)
	ARGUS tower	Three-level mean meteorology and 3D sonic turbulence, one-level LI-COR H ₂ O
	2× ARL wind lidar	3D wind profiler (<i>u</i> , <i>v</i> , <i>w</i>)
	2× beach flux tripod	Two-level <i>T</i> and RH and 3D sonic anemometers, LI-COR H ₂ O on one tower
Yardim	UWB emitters	EM signal strength in UWB frequencies
Horgan/Wiss	Calibrated emitters	RF beacons in S, C, and X bands, sources for offshore receivers
	Soundings + meteorology	Vertical profiles of <i>T</i> , RH, <i>p</i> , and wind and surface weather station
Hanley et al.	AEAS weather station	Automated Environmental Assessment System with masts on both sides of pier and IR SST sampling
	527 and 1,047 nm lidars*	Aerosol distribution, cloud heights, backscatter cross sections, and extinction (visibility)
	FTIR	Spectral radiance 2–12 mm for vertical profiles of <i>T</i> , RH, and <i>p</i> up to <2 km, SST, and possibly salinity
	CIMEL sun photometer*	Path-integrated aerosol optical depth for 340–1,640 nm
	VIS/NIR spectrometer	Grating spectrometer for spectral radiance, 0.5–0.9 μm
	GRIMM*	Portable aerosol spectrometer for particle size concentration
	SWIR camera system*	Imager telescope for 0.9–1.7 μm
	MWIR and LWIR camera systems*	Imagery calibrated for background radiance, 3–5 and 8–9.5 μm
	DIMM optical turbulence*	Multiple links of optical Cn ₂ parameter measurements
	Tethered balloon	Small tethered balloon with mean meteorological sensors
	EM beacons	RF transmitters (C and W bands) for offshore receivers

when sea conditions allowed, while microstructure and turbulence dissipation of the upper ocean were measured from *AE*.

CASPER-East also sampled through and above the MABL with different platforms/sensors. Coordinated rawinsonde launches on *HRS*, *AE*, and the shore site were made during all RF sampling periods, providing environmental refractivity profiles along the range of the propagation link. Scanning Doppler lidar wind measurements were included in the experimental design to record along-beam wind profiles in a swath scanned by the lidar. The lidar used a newly designed stabilized platform to minimize beam swerving due to ship motion. Lidar data were used to monitor internal boundary layer development and the associated trapping layer at discontinuities since the gradients of temperature and humidity associated with internal boundary layers have a strong influence on EM ducting (Atkinson and Zhu 2001; Kullessa et al. 2017).

Boundary layer profiling to the lowest few hundreds of meters was also made by a tethered balloon system on board the *AE* to sample the mean wind, temperature, and humidity.

Two types of RF propagation measurement modules were used: transmitting and receiving between the shore site and *AE* while *AE* moved toward the shore [hereafter inbound ship-to-shore link (IBD)], and between the two ships [hereafter ship-to-ship rapid evolution link (SSR)] when the two ships were headed in the opposite direction along the CASPER track. Figure 6 shows a schematic of the basic setup for both links and the associated environmental measurements. During an IBD (Fig. 6a), *HRS* and the surface supersite focused on environmental and surface-layer turbulence sampling between the shore-site transmitters and *AE* using rawinsondes and ASI sampling modules. While *AE* cruised toward the shore transmitters, *HRS* also moved toward shore

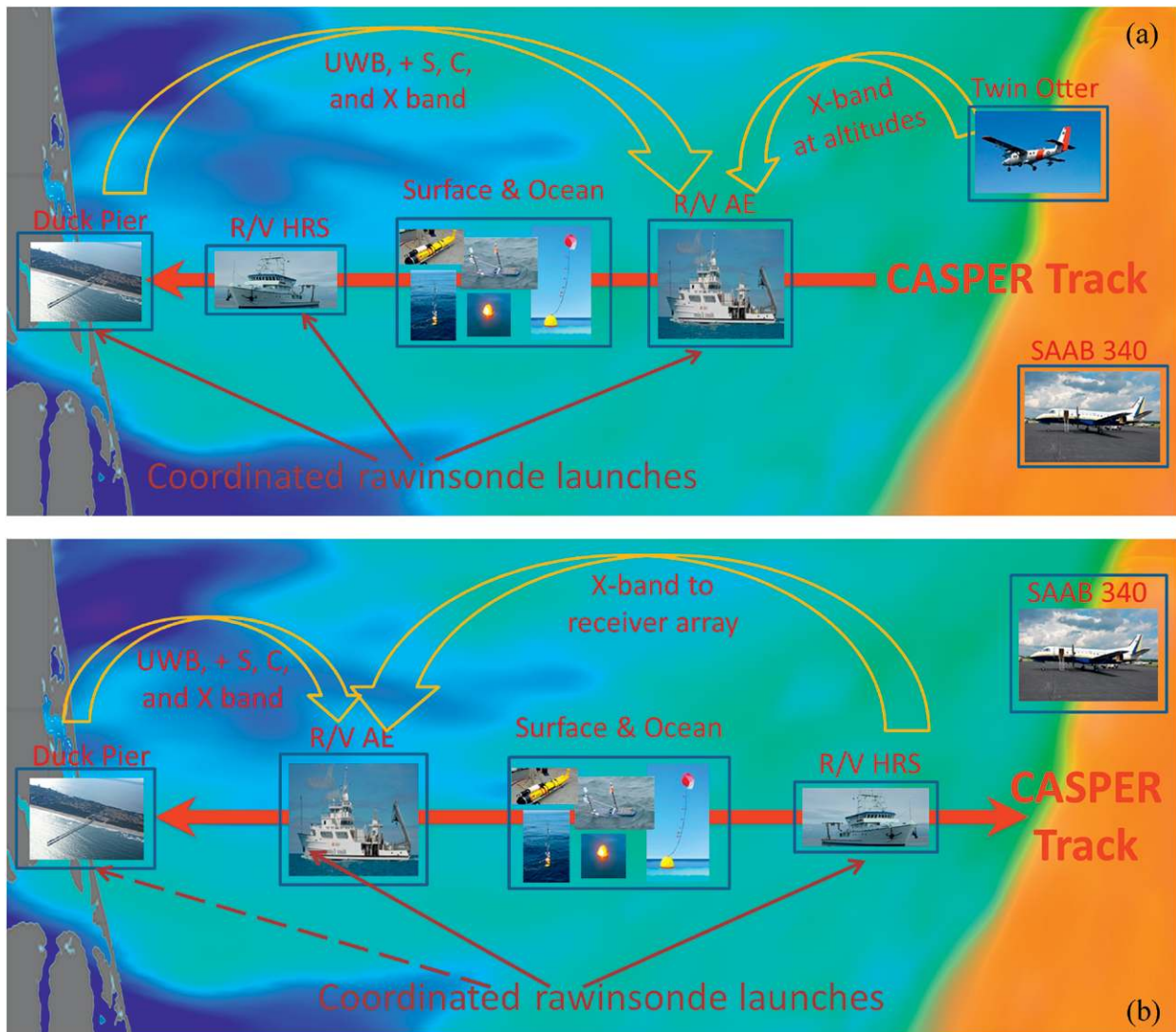


FIG. 6. Illustration of multiplatform coordinated measurement modules for range-dependent RF propagation and environmental sampling: (a) IBD module and (b) SSR module. In the IBD module, the HRS made measurements between the surface supersite and Duck pier while AE covered the entire CASPER track.

at the same time and speed, covering the environmental sampling between the surface supersite and the shore. This setup halved the time it would have taken for a single ship to sample the entire propagation path. During an IBD, ASIs from both ships were made at the start of the module, normally with AE at R30 and HRS at R16, and when each ship reached about R2, about 2 nautical miles (n mi) from shore. The SSR (Fig. 6b) and associated meteorological and oceanic measurements are illustrated. In SSR, AE was normally set to head toward shore so the ship-to-shore link at multifrequencies was also measured in addition to the X-band ship-to-ship link. In both SSR and IBD modules, AE tuned to receive X-band signals from the CTV when the aircraft was aft and heading toward AE, allowing sampling of the X-band

signal from a transmitter at variable altitudes. On the outbound AE transit path, the X-band receiver on AE measured signals from the calibrated transmitter on the shore site (Table 1, Fig. 6).

Figure 7 shows the ship tracks and all sampling modules made on 16 and 17 October 2015 to illustrate the sampling strategy of CASPER-East using the two ships in synchronized transits to execute the IBD and SSR modules. An IBD typically lasted about 5 h while an SSR took half the time of an IBD with the ships moving in opposite directions. Usually, one IBD and two SSRs could be completed in a 24-h period, although the nighttime SSR did not have supporting data from the small platforms for safety reasons. In the example from 16 to 17 October 2015 (Fig. 7), there were five coordinated soundings and four ASIs along the

propagation path during the IBD module in the morning hours, four soundings and two ASIs in the first SSR, and five soundings and one ASI during the second SSR. Twin Otter measurements started on this day at around 1100 eastern daylight time (EDT), making measurements along the same path as the ships.

The EM link measurements on *AE* are denoted on each section of the *AE* transit in Fig. 7. There were five range-dependent measurements conducted on this day. During the IBD, the ultrawide band (UWB) and X-band links between *AE* and the Duck pier were made. Once the TO was in the air, the receiver on *AE* tuned to the X-band transmitter on the CTV, while the UWB link continued whenever *AE* headed toward shore. When *AE* headed away from shore, it measured the propagation of the shore-site X-band transmitter. Finally, *AE*-to-*HRS* X-band propagation measurements were measured during the second SSR module. The measurement scenarios shown in Fig. 7 illustrate the CASPER sampling strategy to maximize the ship and aircraft time for optimal measurements of RF propagation and the corresponding air–sea environment. Throughout the CASPER-East IOP, the two ships made a total of 17 IBD and 31 SSR evolutions. Table 3 lists measurements of major CASPER platforms/sensors for each day during the IOP.

PREVAILING METEOROLOGICAL AND OCEANIC CONDITIONS DURING CASPER-EAST. Several synoptic systems moved through the CASPER-East region during the IOP as depicted in Fig. 8. The cold-frontal passage on 18 and 19 October brought sustained northerly winds of 10–14 m s^{−1} with cold, dry air (~12°C) over the warm (~20°C) ocean. Waves/swell grew to ~2 m in significant wave height (Hs). The strong dynamic forcing gradually diminished during the day on

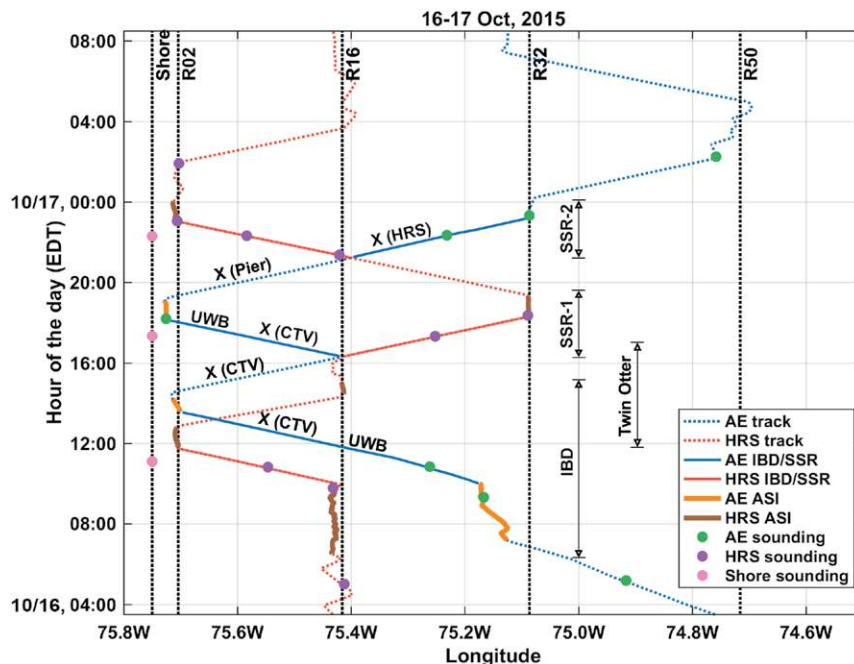


FIG. 7. Coordinated ship, shore, and aircraft measurements on 16 and 17 Oct 2015 showing the longitudinal evolution of *AE* and *HRS* along the CASPER track at latitude 36.1837°N (blue and pink lines). The periods of coordinated measurements (IBD or SSR) are highlighted in solid lines of the same color and are also noted to the right. The time period of TO/CTV flight is also noted to the right. Time and location of soundings from *AE*, *HRS*, and Duck pier are shown as dots; those of the ASI modules are shown as thick lines. The measured EM links are noted along the *AE* track to denote the frequency bands (X or UWB) and the transmitter-hosting platform for this link. Note both X-band and UWB receivers were on *AE*. The distances from the Duck pier are noted at the top of the figure as Rxx, where the numbers denote distances from the pier in nautical miles.

19 October, while the air mass over the CASPER region remained exceptionally cold and dry until 20 October. Two other cold fronts moved through on 23 and 26 October, both with 10–12 m s^{−1} wind and moderately cool and dry air. On 28 October, the CASPER region experienced a rigorous warm-frontal passage that brought warm and moist air to the area with rainfall in the early morning. The winds built a rough sea from the south on top of a southeast swell, which was persistent through 29 October (Fig. 8e). Unfortunately, the strong wind–wave conditions made it impossible to deploy and recover small platforms from the ships during these periods. More complete measurements were made on relatively calm days (Table 3). Although the two ships were generally separated during the measurement period, the differences in their measurements of mean wind, temperature, and humidity were generally small over the shelf region, except during the GS missions between 29 October and 1 November 2015, suggesting stronger spatial variability over the GS (Fig. 8). Figure 8c also

TABLE 3. Availability of measurements from different platforms/sensors during CASPER-East. The NPS tethered-balloon system on the work boat of the R/V Sharp is referred to as the Marine Atmospheric Profiling System (MAPS). The rows of “X band,” “18–40 GHz,” and “<18 GHz” give the days with received signals at X-band antenna array and at the high- and low-frequency ranges of the UWB system, respectively. The last row denotes the days with the S-, C-, and X-band emitters at the pier. The R/V Hugh R. Sharp was on port call on 22 Oct and part of 28 Oct 2015. Measurements of all moving or relocatable platforms were deployed at the Gulf Stream between the evening of 29 Oct and midnight of 1 Nov 2015.																																	
Platform/sensor	October										November																						
	13	14	15	16	17	18	19	20	21	22	23	24	25	26	27	28	29	30	31	1	2	3	4	5	6								
AE	●	●	●	●	●	●	●	●	●	●	●	●	●	●	●	●	●	●	●	●	●	●	●	●	●	●	●	●	●	●	●	●	
HRS	●	●	●	●	●	●	●	●	●	●	●	●	●	●	●	●	●	●	●	●	●	●	●	●	●	●	●	●	●	●	●	●	●
Pier	●	●	●	●	●	●	●	●	●	●	●	●	●	●	●	●	●	●	●	●	●	●	●	●	●	●	●	●	●	●	●	●	●
Twin Otter	●	●	●	●	●	●	●	●	●	●	●	●	●	●	●	●	●	●	●	●	●	●	●	●	●	●	●	●	●	●	●	●	●
SAAB 340	●	●	●	●	●	●	●	●	●	●	●	●	●	●	●	●	●	●	●	●	●	●	●	●	●	●	●	●	●	●	●	●	●
MASFlux	●	●	●	●	●	●	●	●	●	●	●	●	●	●	●	●	●	●	●	●	●	●	●	●	●	●	●	●	●	●	●	●	●
Wave buoys	●	●	●	●	●	●	●	●	●	●	●	●	●	●	●	●	●	●	●	●	●	●	●	●	●	●	●	●	●	●	●	●	●
MAPS	●	●	●	●	●	●	●	●	●	●	●	●	●	●	●	●	●	●	●	●	●	●	●	●	●	●	●	●	●	●	●	●	●
X band	●	●	●	●	●	●	●	●	●	●	●	●	●	●	●	●	●	●	●	●	●	●	●	●	●	●	●	●	●	●	●	●	●
18–40 GHz	●	●	●	●	●	●	●	●	●	●	●	●	●	●	●	●	●	●	●	●	●	●	●	●	●	●	●	●	●	●	●	●	●
<18 GHz	●	●	●	●	●	●	●	●	●	●	●	●	●	●	●	●	●	●	●	●	●	●	●	●	●	●	●	●	●	●	●	●	●
S, C, X band	●	●	●	●	●	●	●	●	●	●	●	●	●	●	●	●	●	●	●	●	●	●	●	●	●	●	●	●	●	●	●	●	●

shows short periods of stable stratification (air temperature warmer than SST) while most measurements were made in unstable boundary layers.

Surface-layer fluxes of momentum τ , sensible heat (SHF), and latent heat (LHF) from both ships are important MASL parameters to be used in validating and improving ED models as well as mesoscale models. Measured surface fluxes are also critical parameters in addressing the energy balance in the upper ocean in order to understand the air–sea coupling processes. Figure 9 shows strong spatial and temporal variations associated with the frontal passages and the GS during the entire IOP. The storm on 18 and 19 October produced SHF and LHF reaching ~ 160 and 300 W m^{-2} , respectively, as cold, dry air and moderate to high winds passed over relatively warm water (see Fig. 8). Similar elevated fluxes were observed during the other two frontal passages (23 and 26 October). Surface fluxes over the GS (29 October–1 November) are in the ranges of $50\text{--}100$ and $200\text{--}400 \text{ W m}^{-2}$ for SHF and LHF, respectively, much higher than those over the continental shelf in nonstorm days.

MEASUREMENT COMPONENTS AND EXAMPLE RESULTS. *EM propagation measurements and analyses.* For EM modeling in CASPER, the parabolic wave equation (PWE) method is used as the primary numerical solution for modeling propagation with more complex M profiles (Dockery 1988; Barrios 1992, 1994). The Advanced Propagation Model (APM), based on PWE, is applied to generate libraries of propagation loss as a function of range for retrieving the M profile from measurements (Barrios 1994). PWE uses a recursive split-step fast Fourier transform (FFT) formula to compute the EM field in complex environments with range and height-varying refractivity $M(r, z)$. PWE computes the vertical EM field at $r + \Delta r$ using the vertical field at the previous range $u(r, z)$ as

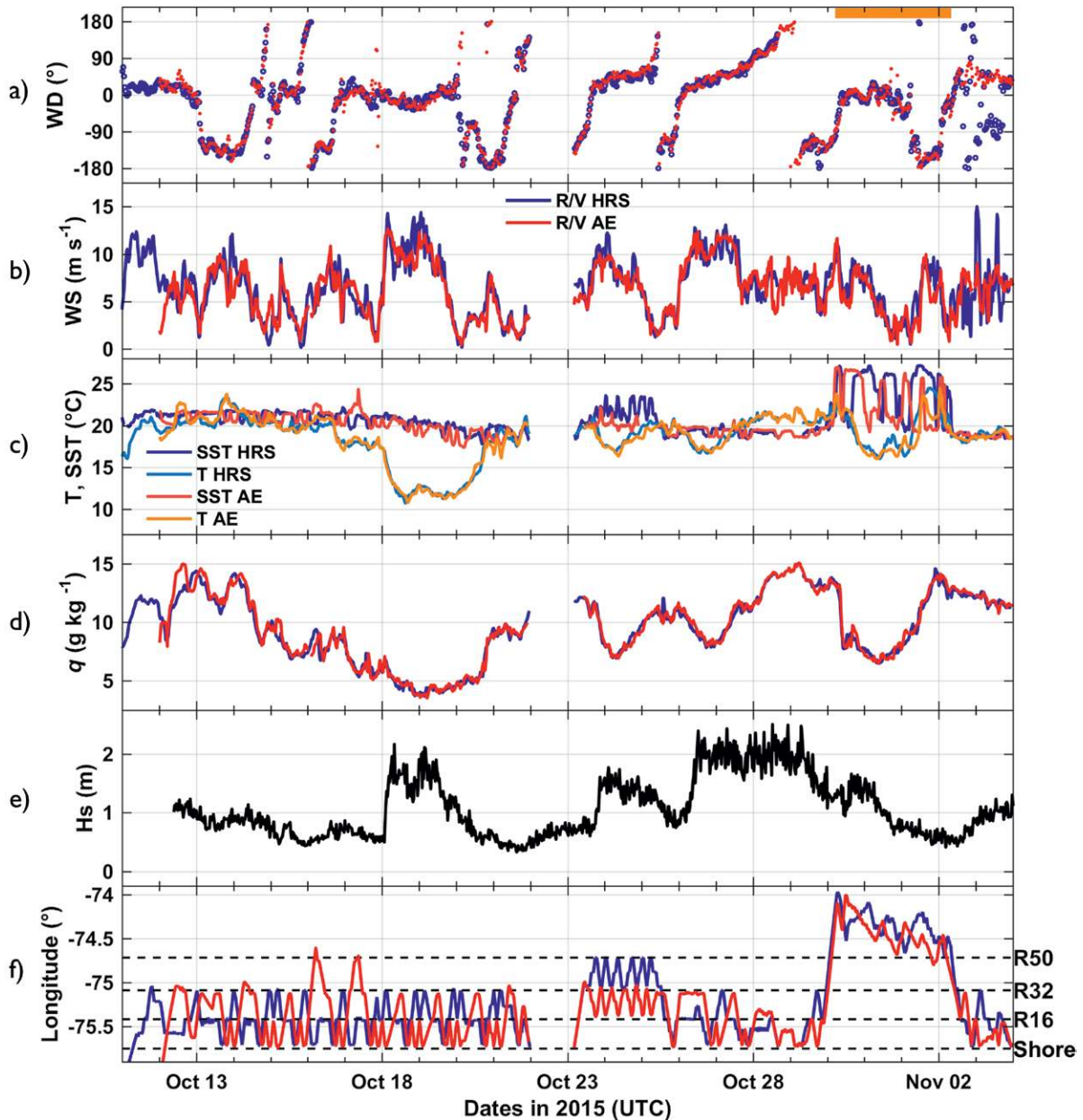


FIG. 8. Meteorological and surface wave conditions observed during CASPER-East IOP: (a) wind direction (WD), (b) wind speed (WS), (c) air temperature T and SST, (d) specific humidity q , (e) significant wave height (H_s), and (f) longitude variation of both ships. All measurements were made on the bow masts of R/V *Hugh R. Sharp* and R/V *Atlantic Explorer*, except for H_s , which was measured by a miniwave buoy at R16. The four dashed lines in (f) denote the longitude of the shore site at Duck, NC, and a few frequently used locations along the CASPER track at 16, 32, and 50 n mi from shore. The orange bar in (a) indicates the period of GS observations. Note that the longitude alone cannot represent the distance to shore for the GS missions as the ship track was along the northwest–southeast direction.

$$u(r + \Delta r, z) = \exp \left[ik_o \Delta r M(r, z) \times 10^{-6} \right] \mathcal{F}^{-1} \left\{ \exp \left[i \Delta r \left(\sqrt{k_o^2 - k_z^2} - k_o \right) \right] \mathcal{F} \left[u(r, z) \right] \right\}, \quad (3)$$

where k_o and k_z are the EM wavenumber and its vertical component, Δr is the range increment in PWE, and \mathcal{F} and \mathcal{F}^{-1} are the Fourier and inverse Fourier transforms. The effects of temperature,

pressure, and humidity are indirectly injected into the EM calculations at each range via the vertical refractivity profiles $M(r, z)$, which are computed using Eqs. (1) and (2).

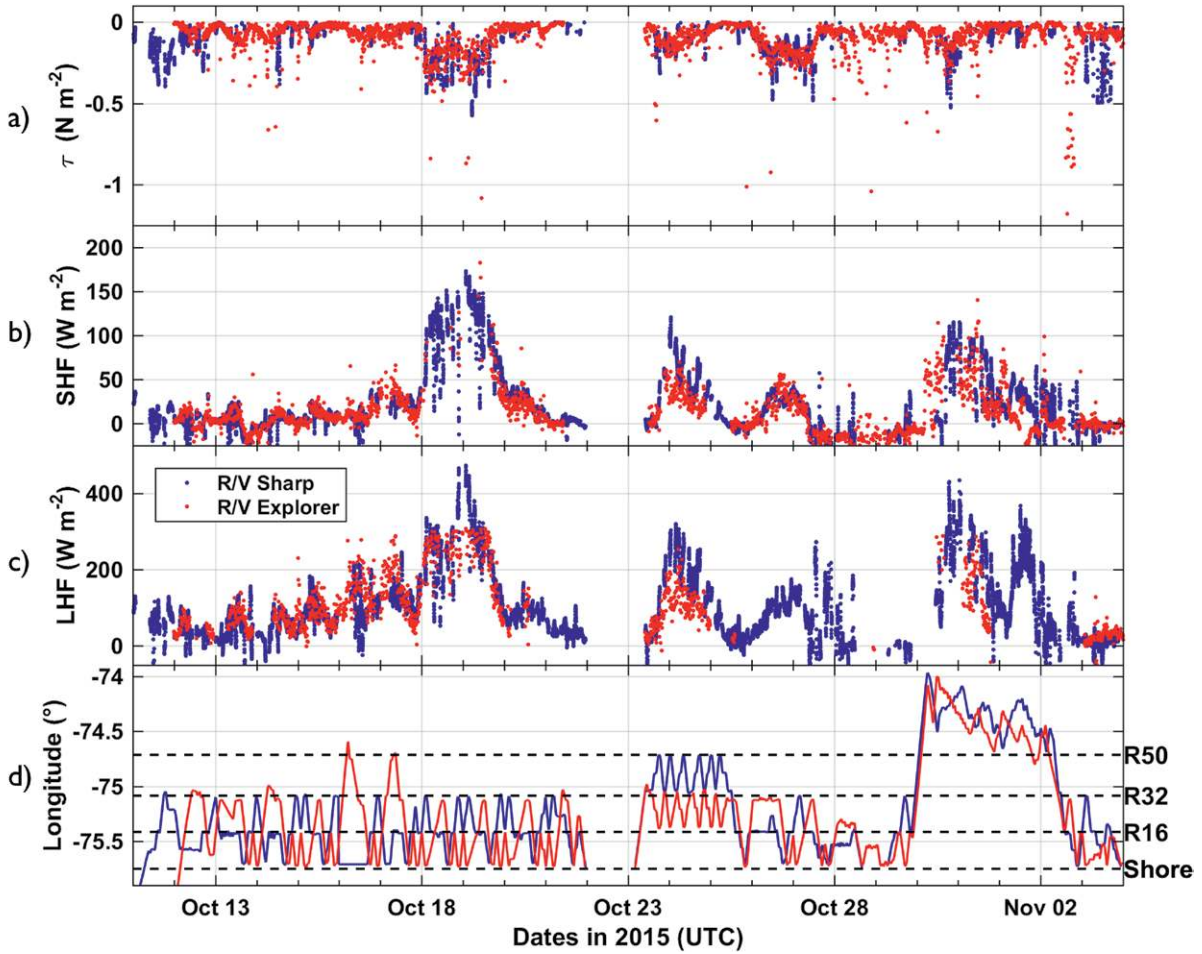


FIG. 9. Turbulent fluxes calculated using the eddy correlation method with high-rate measurements on the bow masts of AE (red) and HRS (blue): (a) momentum flux τ , (b) sensible heat flux, and (c) latent heat flux. Results shown are quality controlled to remove measurements when the wind was outside the $\pm 45^\circ$ sector relative to the ship heading to reduce the effects of flow distortion on flux measurements. (d) Ship locations by longitude.

The propagation loss L (also known as path loss) is a parameter used to quantify the loss of field strength when it propagates from the transmitter to the receiver antenna. For free-space propagation, the received power P_r and free-space loss L_{fs} can be written as

$$P_r = P_t G_t G_r \left(\frac{\lambda}{4\pi r} \right)^2 \text{ with } L_{fs} = \left(\frac{\lambda}{4\pi r} \right)^2, \quad (4)$$

$$\text{so } L_{fs} = \frac{P_r}{P_t G_t G_r},$$

where P_r , G_r , G_t , and λ are transmitted power and antenna gain, receiver antenna gain, and EM wavelength. In a ducted environment, L_{fs} is replaced with propagation loss L in the equation above, and it can be measured from received power P_r . PWE computes L by marching the starter field at $r = 0$ to the receiver range and computing the ratio of fields at receiver and transmitter. Previous work in estimating the

atmospheric conditions from various EM measurements are summarized in Karimian et al. (2011).

Figure 10 shows the measured propagation loss L (dB) from 16 October 2015 from two major CASPER EM links: the X-band receiving array and the UWB multifrequency system. In Figs. 10a–d, L at 10.7 GHz is plotted versus range for each of the receiving antennas mounted at different heights on the aft A-frame of AE for source signals from the pier at Duck, NC. Included in the plots are the measurements and L from the APM for a standard atmosphere (SA) with $\partial M/\partial z = 118 \text{ km}^{-1}$ (Sirkova 2012) and an ED with a constant 10.2 m EDH. This is the mean EDH from the modified Coupled Ocean–Atmosphere Response Experiment (COARE) 3.0 model based on mean temperature T , relative humidity (RH), pressure p , SST, and wind from the HRS bow mast during the SSR-2 (Fig. 7). Figures 10e–h include measured data at four frequencies from the UWB system with the APM

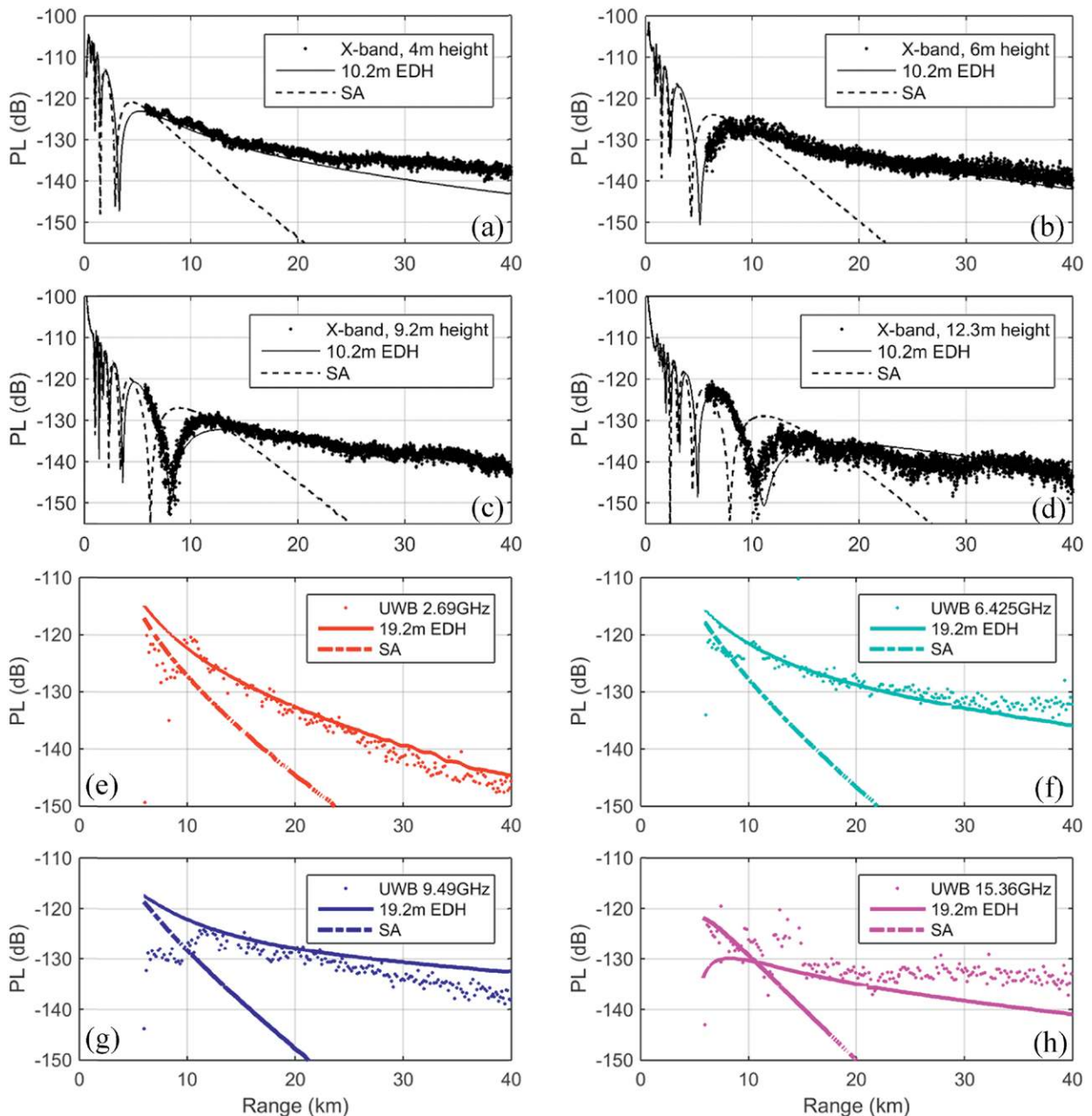


FIG. 10. Typical ship-to-shore propagation loss L at X band (10.6 GHz) for receiving antenna heights at (a) 4.0, (b) 6.0, (c) 9.2, and (d) 12.3 m and from the UWB links at four selected frequencies: (e) 2.69, (f) 6.425, (g) 9.49, and (h) 15.36 GHz. In all panels, the dotted lines are the measured L . The solid and dashed lines are the calculated L from APM using a constant M gradient with $\partial M/\partial z = 118 \text{ km}^{-1}$ with and without an evaporation duct (EDH = 10.2 m) appended to the lowest 100 m, respectively. The different colors denote different frequencies.

results calculated using a constant EDH of 19.2 m from three small-boat profiling measurements during the IBD module. The PWE results indicate less than 25-km detection range in the standard, nonducting atmosphere, while the measured data clearly indicate ducting effects as substantial energy were detected beyond 40 km. For the X-band measurements, the modeled L at 10.2 m seemed to show good agreement

with the measurements, especially for antenna heights at 6, 9.2, and 12.3 m (Figs. 10b–d). At 2.69 or 6.425 GHz (Figs. 10e,f), for example, good agreement is seen at distances shorter than 30 km while the higher frequencies (Figs. 10g,h) show large differences between measured and modeled values. Note that the model assumed a homogeneous atmosphere in this calculation while the ship-based measurements

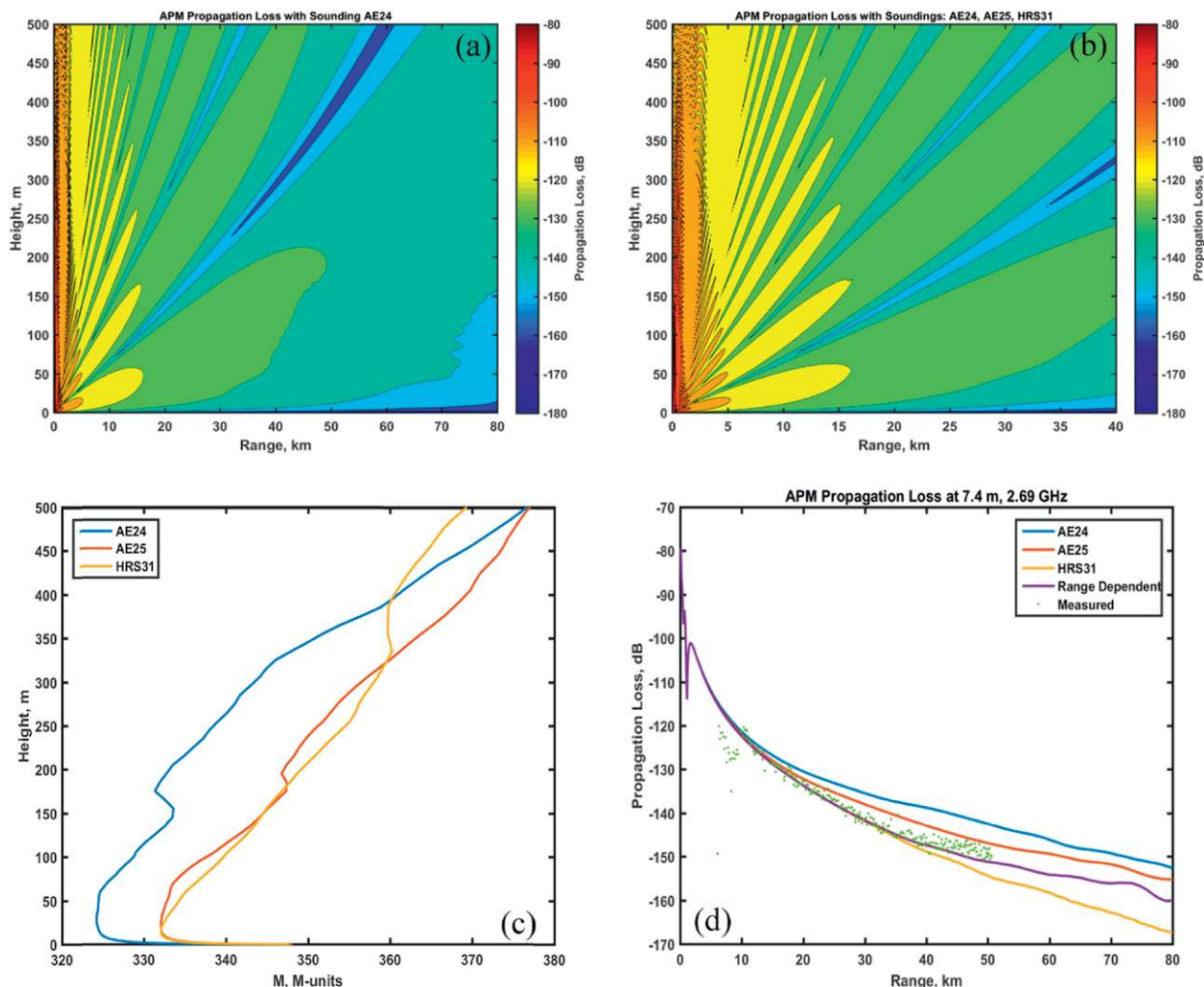


FIG. 11. Simulated propagation loss as a function of height and distance from the pier on 16 Oct 2015 assuming (a) a horizontally homogeneous atmosphere using sounding AE24 and (b) a heterogeneous atmosphere using all three soundings along the CASPER track. (c) A comparison of the M profiles used in the APM simulations. (d) A comparison of the propagation loss between homogeneous and heterogeneous atmospheres and the measured propagation loss. Soundings HRS31, AE25, and AE24 are at 18, 44, and 52 km from shore, respectively. All soundings were modified to include an evaporation duct generated using a nudging method and a single-column model with a surface layer based on MOST (Cherrett 2015).

suggested EDH increased from ~ 13 m near shore to ~ 19 m at the end of the sampling module. This spatial variability is much larger than during the later SSR-2, which is likely the reason for disagreement.

The impact of spatial heterogeneity in atmospheric refractivity on RF propagation is illustrated in Fig. 11, where L at 2.69 GHz at different ranges and heights are depicted for the transmitter at the pier. The input M profiles to the APM are given in Fig. 11c from soundings HRS31, AE25, and AE24 at 18, 44, and 52 km from the shore site. Each of the original sounding profiles was blended with an evaporation duct profile based on MOST using a nudging method proposed by Cherrett (2015) in order to combine

the modeled surface layer with higher-level profiles based on soundings. The resulting blended soundings indicated EDHs of 13.8, 21.3, and 23.8 m for HRS31, AE25, and AE24, respectively, to represent the horizontal variability along the propagation path. Figure 11a shows L as a function of height and range using the AE24 sounding and assuming a homogeneous atmosphere. Figure 11b is similar to Fig. 11a except that all three soundings were used as input to APM at their respective range from shore. Figure 11b shows L using range-dependent M profiles, although the range resolution was rather coarse. Figure 11d shows the variations of L at 7.4-m receiver height from four simulations, three with a homogeneous

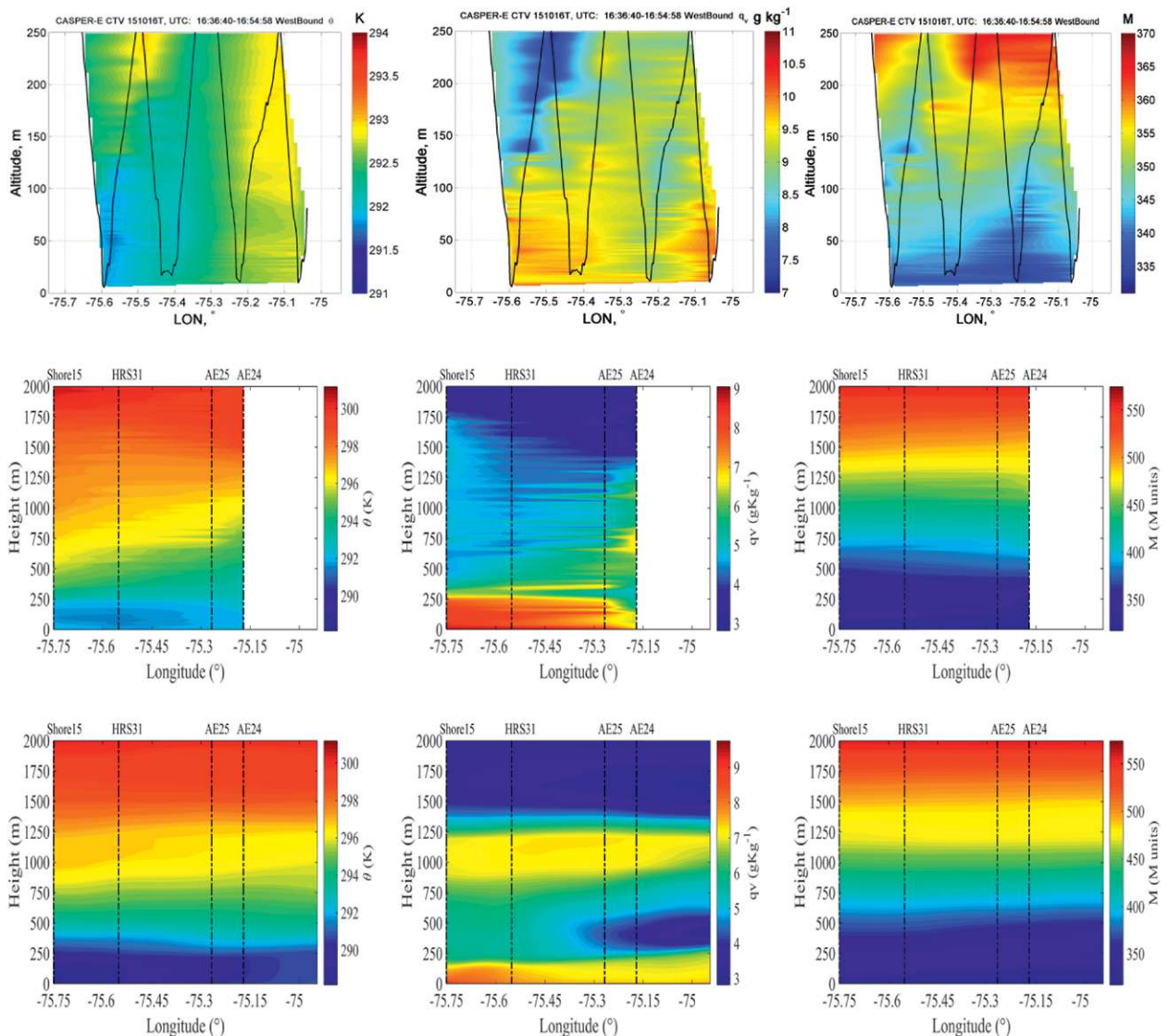


FIG. 12. Vertical cross section of (left) potential temperature θ , (center) specific humidity q_v , and (right) modified index of refraction M as a function of longitude on 16 Oct 2015. (top) Results from the CTV tethered to the Twin Otter for the lowest 250 m, (middle) interpolated values using coordinated soundings from the two ships and the shore site, and (bottom) results from COAMPS simulation on the same day. The vertical dashed lines in the sounding and COAMPS plots denote the locations of the soundings with ship names and sounding numbers shown on the top axis.

atmosphere assumption using each of the profiles in Fig. 11c. The purple line in Fig. 11d is the result of simulation using all profiles at their respective ranges. Figure 11d shows substantial differences for L in the homogeneous atmosphere simulations using individual soundings. At the 50-km range, the difference in L between the HRS31 and AE24 soundings is more than 10 dB. This is an expected result since the EM propagation is sensitive to $\partial M/\partial z$: for example, the larger the magnitude of $\partial M/\partial z$, the more the EM signal is bent toward the ground with full trapping occurring at negative values. When calculating the gradients of

M ($\partial M/\partial z$) based on the M profiles in Fig. 11c, we found a larger magnitude of $\partial M/\partial z$ in AE24 and AE25 than HRS31 within the first 100 m. This resulted in the EM signal bending downward, leading to a larger measured signal and a smaller L compared to the HRS31 profile. As the range-dependent profile is a mixture of these, the propagation loss lies between the AE24/AE25 and HRS31 results, and it matches well with the measured data. Since both transmitters and receivers were at low altitudes (~ 10 m), M profiles above the surface layer will have a much smaller effect. It is clear from Fig. 11 that the simulation for

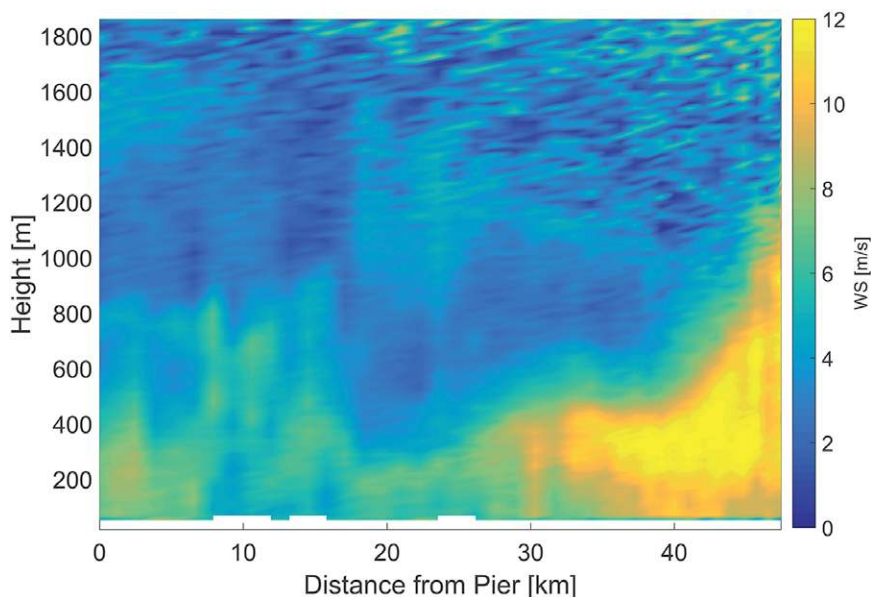


FIG. 13. Vertical cross section of wind speed as a function of distance from the pier at 1337–1729 UTC 16 Oct 2015. The measurements were made by a scanning lidar on a stabilized platform on AE.

the heterogeneous atmosphere matched the measured L the best. These results support the CASPER focus on range-dependent refractivity characterization in a heterogeneous atmosphere.

Atmospheric refractivity and air–sea interaction sampling.

The coordinated measurements from AE, HRS, the shore site, and the aircraft on 16 October 2015 are shown in Fig. 12. During the IBD in the morning hours, five rawinsonde launches were made along the CASPER track (Fig. 7). There was also a TO flyover at the end of the IBD with the CTV porpoising (up and down pattern) along the CASPER track in the lowest 300 m of the boundary layer. CTV measurements show strong horizontal and vertical variability in the lowest 250 m of the atmosphere (Fig. 12, top row). Sounding data show similar trends of variation in water vapor where the easternmost sounding from AE sampled the driest low-level air, consistent with the CTV data in the vicinity. The progressively cooler air toward the west in the lowest 250 m is also observed in both the sounding and the CTV measurements (note the difference in the color range between the two datasets). However, one should not expect the soundings and the CTV to show exactly the same results because of differences in spatial resolution and a time difference of about 4 h. The COAMPS results (bottom row) reveal the presence of low-level cool and moist air and the dry layer above 1,300 m, in good agreement with the rawinsonde profiles. The M vertical cross sections from COAMPS and interpolated from soundings compare very well,

which is the case for many days during CASPER-East. A detailed evaluation of COAMPS performance in CASPER-East and the mesoscale variability of refractivity are given in Ulate et al. (2018, manuscript submitted to *J. Appl. Meteor. Climatol.*).

A comparison between the M field computed from the TO measurements and the soundings reveals the finescale structure of the modified refractivity in the aircraft measurements that are not present in the five soundings along the path or the COAMPS results. These aircraft measurements in CASPER-East and

the concurrent RF L measurements between the CTV and AE provide a unique dataset to help understand the impact of “troposcatter” that accounts for the effects of turbulence-scale refractivity variations (Kulesa et al. 2017).

Figure 13 shows the lidar measurements of the boundary layer winds from the AE during the IBD on 16 October 2015. Westerly winds persisted throughout the inbound run before shifting to more northerly when AE was approximately 10 km from shore. Even for this seemingly simple case the wind profile evolution is complex, and interpretation requires delineation of space–time information contained in onboard lidar measurements. From 50 to 30 km from the shore, a westerly jetlike flow prevailed, its upper edge descending rapidly with distance (and time) from 1.2 km to 400 m, followed by dissolution of the jet as AE traversed onshore of 20 km. Similar wind development was also observed in the coordinated sounding plots and COAMPS (not shown). Ongoing research includes identification and understanding causality of internal boundary layers at discontinuities (land–ocean interface) and their implications in EM ducting.

CASPER made the first attempt to sample T , RH, and p profiles in the MASL using a tethered-balloon-based sampling system from a small boat. The small boat introduced minimal disturbance to its immediate environment and allowed repeated profiling down to ~ 0.5 m MSL. Figure 14 shows results from four sets of profiles representing different thermal stability conditions denoted by air–sea temperature

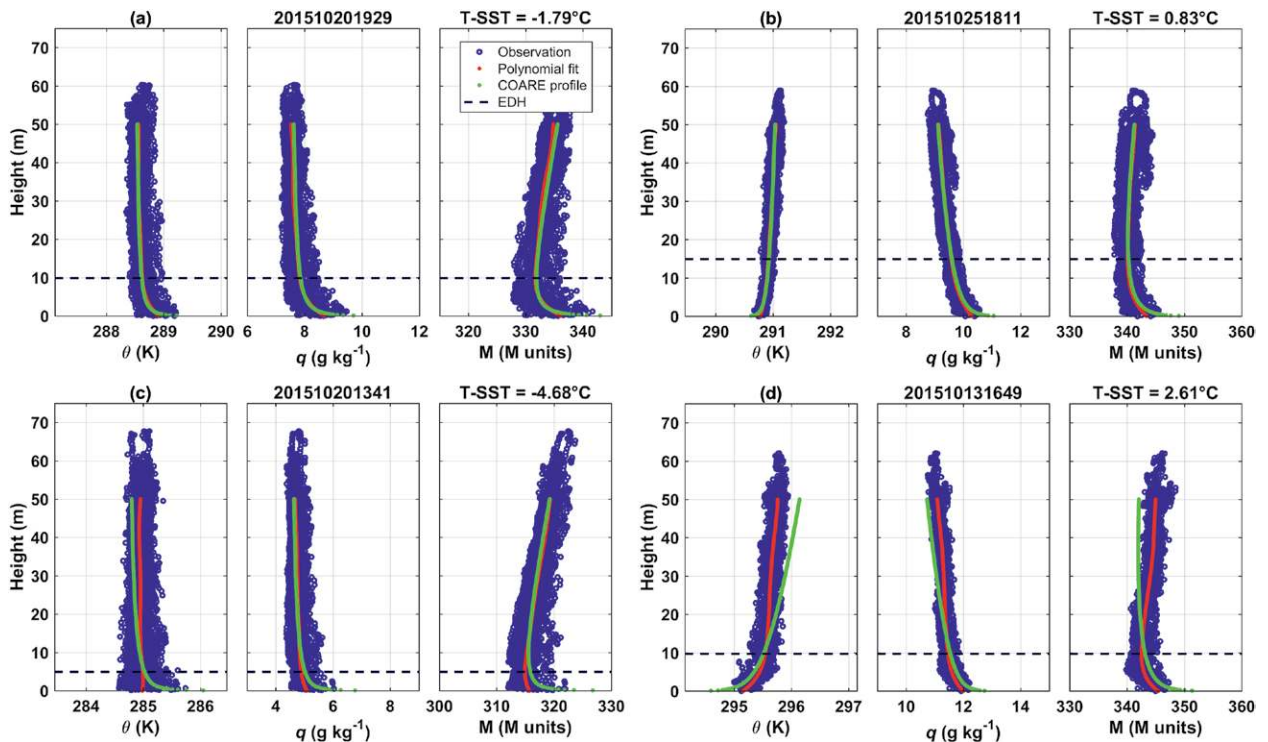


FIG. 14. Vertical profiles of θ , q , and M obtained from MAPS. The data were collected during a period of 30–45 min consisting of nominally seven upward and seven downward profiling measurements. In each panel, the red line is a seventh-order polynomial fit to the observed data and the green line is the MOST-following profile using mean temperature and RH at 10-m height and the mean wind from the nearby HRS. The horizontal dashed line denotes the EDH level obtained from the mean M profile. The four sets of data [i.e., (a)–(d)] are examples of different thermal stability denoted by the air–sea temperature difference ($T - \text{SST}$) for each case, where T is the mean temperature at 10-m height and SST is the calibrated SST from the nearby HRS.

difference (ASTD). The scattering seen in all profiles is expected given the turbulent nature of the MASL and suggests the uncertainty associated with using a single sounding to represent the MASL conditions. In spite of the scatter, the strong gradients near the surface in all mean profiles, especially in q (and hence M), are clear in all cases. From the four measured mean M profiles, the EDHs are 9.9, 14.9, 4.9, and 9.7 m for cases in Figs. 14a–d, respectively.

The COARE profiles in Fig. 14 were calculated based on the COARE 3.0 algorithm (Fairall et al. 1996, 2003) modified to output vertical profiles of the MASL (Alappattu et al. 2016). Inputs to the COARE algorithm included mean T , p , and RH in the altitude range of 10 ± 0.5 m from the measurements, mean wind from HRS's bow mast at 12 m, and SST from HRS averaged for the period of corresponding tethered-balloon measurements.

Figures 14a and 14b show good agreement between measured and COARE profiles. These are cases with moderate ASTD in unstable and stable stratification conditions, respectively. For the unstable case with a larger magnitude of ASTD

(-4.68°C ; Fig. 14c), θ below 20 m shows larger variability than the layer above with no clear trend in the vertical gradient. The increase of q toward the surface is still observed, although it is much weaker compared to the COARE profile. In the strongly stable case (Fig. 14d), significant deviations in the θ and q profiles are apparent. These findings need to be examined further with more observed cases in order to make general conclusions.

Upper-ocean measurements. Upper-ocean mixing and advection affect EM ducting by regulating the SST variability, which was identified as one of the critical factors for accurate predictions of coastal refractivity (Haack et al. 2010). Extensive upper-ocean temperature, salinity, and turbulence parameters were sampled in CASPER-East from both ships as listed in Table 1. Figure 15 shows the thermohaline and microstructure measurements collected on the North Carolina shelf between 13 and 21 October 2015, indicating oceanic stratification on the shelf was influenced by highly variable surface salinity and along-bottom advection. The wind-induced

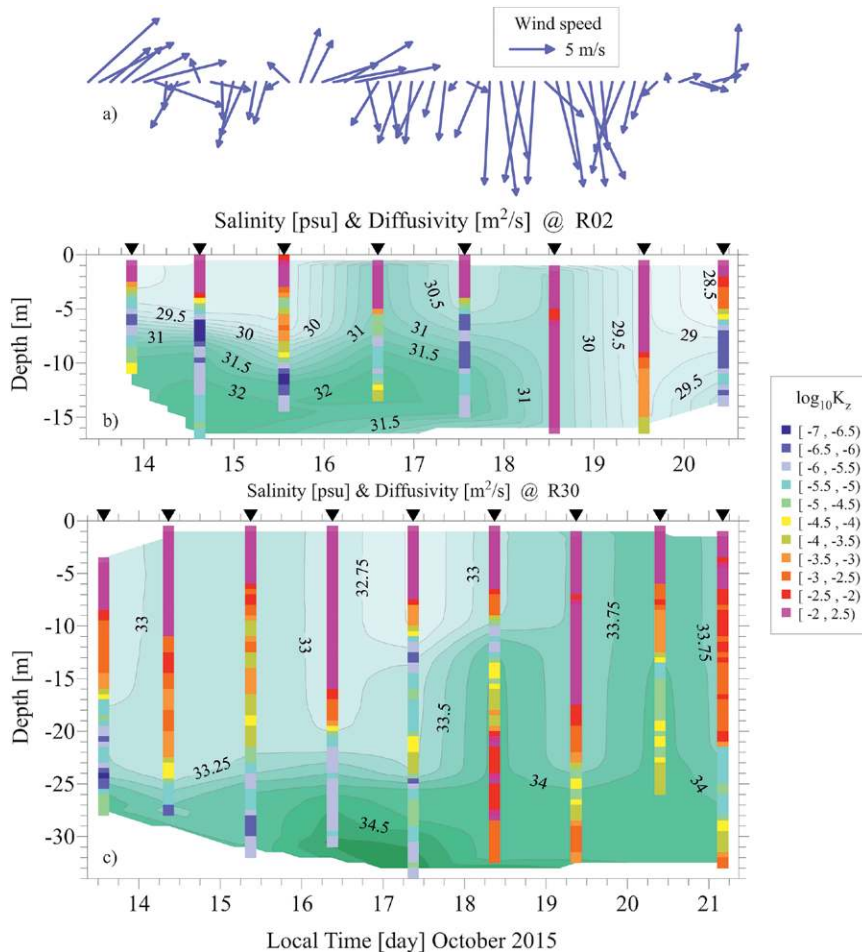


FIG. 15. (a) The time-averaged (every 3 h) wind vectors $\mathbf{W}_0(t)$ measured from R/V *Atlantic Explorer* and salinity contour plots at (b) R02 and (c) R30 overlaid by the eddy diffusivity profiles $K_z(z)$.

turbulence, which was dominant on the NC shelf, produced vertical mixing that can be quantified by the diffusivity profiles $K_z(z)$ shown in Fig. 15 (overlaid on the background of salinity contours) for the nearshore station R02 and the midshelf station R30, respectively. The surface salinity measured at 3 m below the sea surface depicts substantial spatial variations along the track between R02 and R30 (Figs. 15b,c). The difference of salinity between relatively fresh coastal (R02) and more-saline midshelf (R30) waters was about 4 practical salinity units (psu) on average. Passing storms may play a significant role in the midshelf salinity variation. Figure 15b shows nearly constant salinity during the first 3.5 days of observations (~ 33 – 33.1 psu), increasing to ~ 33.6 – 34 psu after the peak of the 18 October frontal passage (see Figs. 15a and 8). Near the coast, however, salinity steadily increased from 28.8 to ~ 30 psu. After the frontal passage on 18 October, it rapidly decreased to 28 psu on 20 October

when the northerly winds ceased. The observed spatial-temporal variations of salinity on the inner shelf were mostly caused by alternate advection of relatively fresh estuarine and highly saline ocean water on the shelf, depending on the direction of dominant winds.

On the midshelf, the diffusivities in the water interior spanned over five decades during the observational period, from $\sim 10^{-6}$ to $\sim 10^{-1} \text{ m}^2 \text{ s}^{-1}$. The midshelf eddy diffusivities are characterized by the median value $\hat{K}_z \sim 5 \times 10^{-4} \text{ m}^2 \text{ s}^{-1}$, which is comparable with the values in other shelf regions. Lozovatsky et al. (2017) describe the calculations of K_z from the measured dissipation rate and give more detailed analyses on the upper-ocean mixing and advection during CASPER-East.

Sea surface temperature is one of the critical inputs to evaporation duct models. During CASPER-East, calibrated skin temperature measurements were made on board *HRS* using an infrared SST autonomous radiometer (ISAR). This dataset was used to correct the bulk water temperature from ship water-intake measurements (Alappattu et al. 2017a). Spatial variability of the SST was also mapped by the Twin Otter and CTV from low altitudes and by the SAAB 340 using radiometric measurements. In addition, all SST measurements in CASPER-East were consolidated into an SST database by multiple CASPER groups using the *HRS* SST from ISAR to calibrate all airborne, buoys, and ship-based measurements to represent the true skin temperature (Alappattu et al. 2017b).

SUMMARY. CASPER is a multidisciplinary coordinated effort aimed at improving our understanding of air–sea interaction processes in the MABL resulting in anomalous propagation of EM energy. The ultimate goal of CASPER is to enhance our

capability to predict anomalous propagation over a range of order ~100 km that relies on adequate depictions of the atmospheric surface layer gradients and the MABL inversion strength within the domain of interests. CASPER-East was the first of two field campaigns to address issues of boundary layer spatial heterogeneity on EM propagation. Coordinated measurements by two ships, two research aircraft, a shore site, and multiple at-sea buoys and autonomous vehicles were used to sample both the upper-ocean and atmospheric boundary layer refractive conditions in conjunction with range-dependent EM propagation measurements. The sampling was repeated along the same track over the continental shelf region using two basic coordination modules for concurrent refractivity, air-sea interaction, and propagation measurements. This technique yielded a wealth of data for process studies, testing of new theories on surface-layer development and on coastal internal boundary layer development, model evaluation, and model improvements. Initial results on air-sea interactions were presented at the CASPER special session at the 20th Conference on Air-Sea Interaction in Madison, Wisconsin, in August 2016 sponsored by the American Meteorological Society. A second CASPER special session was held at the January 2017 National Radio Science Meeting sponsored by the U.S. National Committee of the International Union of Radio Science (URSI). The majority of the data are quality controlled and available for collaborative analyses.

ACKNOWLEDGMENTS. CASPER thanks the funding support of the Office of Naval Research (ONR) under its Multidisciplinary University Research Initiative (MURI) program, Grant N0001416WX00469, under project managers Dr. Daniel Eleuterio and Steven Russell, and the additional support for CASPER collaborators from ONR and from NRL Program Element 61153N (WU BE023-01-41-1C04). We also thank the crews of the R/V *Atlantic Explorer*, R/V *Hugh R. Sharp*, and the CIRPAS Twin Otter and all participants of the CASPER field campaign for their hard work in the field. The efforts of many students, Alex Olson (Moss Landing Marine Lab); Nathan Rose and Ross Palomaki (University of Virginia); Evan Ntonados (Millersville University); and Andrew Kammer, Austin Waldorf, and Patrick Mears (Coastal Carolina University) are gratefully acknowledged. We thank Carlos Fierro from SPAWAR San Diego for monitoring the NPS Wave Glider, David Grober from Motion Picture Marine and Cliff Hudson from Emerging Technologies Inc. for rapidly designing and constructing the LIDAR stabilizing platform, and Orson Hyde for invaluable technical support on the R/V *Atlantic Explorer*.

REFERENCES

- Alappattu, D. P., Q. Wang, and J. Kalogiros, 2016: Anomalous propagation conditions over eastern Pacific Ocean derived from MAGIC data. *Radio Sci.*, **51**, 1142–1156, <https://doi.org/10.1002/2016RS005994>.
- , —, R. Yamaguchi, R. J. Lind, M. Reynolds, and A. J. Christman, 2017: Warm layer and cool skin corrections for bulk water temperature measurements for air-sea interaction studies. *J. Geophys. Res. Oceans*, **122**, 6470–6481, <https://doi.org/10.1002/2017JC012688>.
- , and Coauthors, 2017b: Generating accurate skin sea surface temperature data from observations made using multiple platforms during CASPER field experiment. Naval Postgraduate School Tech. Rep. NPS-MR-17-001, 36 pp., <http://hdl.handle.net/10945/56655>.
- Anderson, K., and Coauthors, 2004: The RED Experiment: An assessment of boundary layer effects in a trade winds regime on microwave and infrared propagation over the sea. *Bull. Amer. Meteor. Soc.*, **85**, 1355–1365, <https://doi.org/10.1175/BAMS-85-9-1355>.
- Atkinson, B. W. and Zhu, M. 2006: Coastal effects on radar propagation in atmospheric ducting conditions. *Meteor. Appl.*, **13**, 53–62, <https://doi.org/10.1017/S1350482705001970>.
- Babin, S. M., G. S. Young, and J. A. Carton, 1997: A new model of the oceanic evaporation duct. *J. Appl. Meteor.*, **36**, 193–204, [https://doi.org/10.1175/1520-0450\(1997\)036<0193:ANMOTO>2.0.CO;2](https://doi.org/10.1175/1520-0450(1997)036<0193:ANMOTO>2.0.CO;2).
- Barrios, A. E., 1992: Parabolic equation modeling in horizontally inhomogeneous environments. *IEEE Trans. Antennas Propag.*, **40**, 791–797, <https://doi.org/10.1109/8.155744>.
- , 1994: A terrain parabolic equation model for propagation in the troposphere. *IEEE Trans. Antennas Propag.*, **42**, 90–98, <https://doi.org/10.1109/8.272306>.
- Battan, L. J. 1973: *Radar Observation of the Atmosphere*. University of Chicago Press, 324 pp.
- Bean, B. R., and E. J. Dutton, 1968: *Radio Meteorology*. Dover Publications, 435 pp.
- Brooks, I. M., A. K. Goroch, and D. P. Rogers, 1999: Observations of strong surface radar ducts over the Persian Gulf. *J. Appl. Meteor.*, **38**, 1293–1310, [https://doi.org/10.1175/1520-0450\(1999\)038<1293:OOSSRD>2.0.CO;2](https://doi.org/10.1175/1520-0450(1999)038<1293:OOSSRD>2.0.CO;2).
- Businger, J. A., J. C. Wynaard, and Y. Izumi, 1971: Flux profile relationships in the atmospheric surface layer. *J. Atmos. Sci.*, **28**, 181–189, [https://doi.org/10.1175/1520-0469\(1971\)028<0181:FPRITA>0.CO;2](https://doi.org/10.1175/1520-0469(1971)028<0181:FPRITA>0.CO;2).
- Chen, S., T. J. Campbell, H. Jin, S. Gaberšek, R. M. Hodur, and P. Martin, 2010: Effect of two-way

- air-sea coupling in high and low wind speed regimes. *Mon. Wea. Rev.*, **138**, 3579–3602, <https://doi.org/10.1175/2009MWR3119.1>.
- Cherrett, R. C., 2015: Capturing characteristics of atmospheric refractivity using observation and modeling approaches. Ph.D. dissertation, Naval Postgraduate School, 185 pp., <http://hdl.handle.net/10945/45825>.
- Dockery, G. D., 1988: Modeling electromagnetic wave propagation in the troposphere using the parabolic equation. *IEEE Trans. Antennas Propag.*, **36**, 1464–1470, <https://doi.org/10.1109/8.8634>.
- Doyle, J. D., and Coauthors, 2012: Real time tropical cyclone prediction using COAMPS-TC. *Advances in Geosciences*, Vol. 28, World Scientific, 15–28, https://doi.org/10.1142/9789814405683_0002.
- , and Coauthors, 2014: Tropical cyclone prediction using COAMPS-TC. *Oceanography*, **27**, 104–115, <https://doi.org/10.5670/oceanog.2014.72>.
- Edson, J. B., C. J. Zappa, J. A. Ware, W. R. McGillis, and J. E. Hare, 2004: Scalar flux profile relationships over the open ocean. *J. Geophys. Res.*, **109**, C08S09, <https://doi.org/10.1029/2003JC001960>.
- Fairall, C. W., E. F. Bradley, J. S. Godfrey, G. A. Wick, J. B. Edson, and G. S. Young, 1996: Cool-skin and warm-layer effects on sea surface temperature. *J. Geophys. Res.*, **101**, 1295–1308, <https://doi.org/10.1029/95JC03190>.
- , —, J. Hare, A. Grachev, and J. Edson, 2003: Bulk parameterization of air-sea fluxes: Updates and verification for the COARE algorithm. *J. Climate*, **16**, 571–591, [https://doi.org/10.1175/1520-0442\(2003\)016<0571:BPOASF>2.0.CO;2](https://doi.org/10.1175/1520-0442(2003)016<0571:BPOASF>2.0.CO;2).
- Frederickson, P. A., 2012: Improving the characterization of the environment for AREPS electromagnetic performance predictions. *Weather Impacts Decision Aids (WIDA) Workshop*, Reno, NV, Desert Research Institute, www.dri.edu/wida-presentations.
- Glaeser, F. J., 1978: Propagation study. Naval Memo. VAW-122, 16 pp.
- Haack, T., C. Wang, S. Garrett, A. Glazer, J. Mailhot, and R. Marshall, 2010: Mesoscale modeling of boundary layer refractivity and atmospheric ducting. *J. Appl. Meteor. Climatol.*, **49**, 2437–2457, <https://doi.org/10.1175/2010JAMC2415.1>.
- Jeske, H., 1971: The state of radar range prediction over the sea. Tropospheric Radio Wave Propagation—Part II, NATO-AGARD Proc. AD719714, 50-1–50-10.
- , 1973: State and limits of prediction methods of radar wave propagation conditions over the sea. *Modern Topics in Microwave Propagation and Air-Sea Interaction*, A. Zanca, Ed., D. Reidel, 130–148.
- Kalogiros, J. A., and Q. Wang, 2011: Aircraft observations of sea-surface turbulent fluxes near the California coast. *Bound.-Layer Meteor.*, **139**, 283–306, <https://doi.org/10.1007/s10546-010-9585-x>.
- Karimian, A., C. Yardim, P. Gerstoft, W. S. Hodgkiss, and A. E. Barrios, 2011: Refractivity estimation from sea clutter: An invited review. *Radio Sci.*, **46**, RS6013, <https://doi.org/10.1029/2011RS004818>.
- Kerr, D. E., 1951: *Propagation of Short Radio Waves*. McGraw-Hill, 728 pp.
- Konstanzer, G. C., 1994: Sensitivity of AN/SPY-1B propagation to evaporation duct heights. JHU/APL Tech. Rep. F2F-94-U-4-012, 34 pp.
- Kulesa, A. S., and Coauthors, 2017: The Tropical Air-Sea Propagation Study (TAPS). *Bull. Amer. Meteor. Soc.*, **98**, 517–537, <https://doi.org/10.1175/BAMS-D-14-00284.1>.
- Lee, T. N., W. J. Ho, V. Kourafalou, and J. D. Wang, 1984: Circulation on the continental shelf of the southeastern United States. Part I: Subtidal response to wind and Gulf Stream forcing during winter. *J. Phys. Oceanogr.*, **14**, 1001–1012, [https://doi.org/10.1175/1520-0485\(1984\)014<1001:COTCSO>2.0.CO;2](https://doi.org/10.1175/1520-0485(1984)014<1001:COTCSO>2.0.CO;2).
- Linder, C. A., and G. Gawarkiewicz, 1998: A climatology of the shelfbreak front in the Middle Atlantic Bight. *J. Geophys. Res.*, **103**, 18 405–18 423, <https://doi.org/10.1029/98JC01438>.
- Lozovatsky, I., J. Planella-Morato, K. Sherman, Q. Wang, and H. S. J. Fernando, 2017: Vertical mixing and elements of mesoscale dynamics over North Carolina shelf and contiguous Gulf Stream waters. *Ocean Dyn.*, **67**, 783–798, <https://doi.org/10.1007/s10236-017-1059-y>.
- Mahrt, L., and D. Khelif, 2010: Heat fluxes over weak SST heterogeneity. *J. Geophys. Res.*, **115**, D11103, <https://doi.org/10.1029/2009JD013161>.
- , D. Vicker, and E. L. Andreas, 2014: Low-level wind maxima in the stably stratified coastal zone. *J. Appl. Meteor. Climatol.*, **53**, 363–376, <https://doi.org/10.1175/JAMC-D-13-0170.1>.
- Makin, V. K., and C. Mastenbroek, 1996: Impact of waves on air-sea exchange of sensible heat and momentum. *Bound.-Layer Meteor.*, **79**, 279–300, <https://doi.org/10.1007/BF00119442>.
- McGillis, W. R., and Coauthors, 2004: Air-sea CO₂ exchange in the equatorial Pacific. *J. Geophys. Res.*, **109**, C08S02, <https://doi.org/10.1029/2003JC002256>.
- Morgan, C. W., and J. M. Bishop, 1977: An example of Gulf Stream eddy-induced water exchange in the Mid-Atlantic Bight. *J. Phys. Oceanogr.*, **7**, 472–479, [https://doi.org/10.1175/1520-0485\(1977\)007<0472:AEOS>2.0.CO;2](https://doi.org/10.1175/1520-0485(1977)007<0472:AEOS>2.0.CO;2).
- Musson-Genon, L., S. Gauthier, and E. Bruth, 1992: A simple method to determine evaporation duct height

- in the sea surface boundary layer. *Radio Sci.*, **27**, 635–644, <https://doi.org/10.1029/92RS00926>.
- Paulus, R. A., 1984: Practical application of the IREPS evaporation duct model. NOSC Tech. Rep. 966, 68 pp., <http://oai.dtic.mil/oai/oai?verb=getRecord&metadataPrefix=html&identifier=ADA146528>.
- , 1985: Practical application of an evaporation duct model. *Radio Sci.*, **20**, 887–896, <https://doi.org/10.1029/RS020i004p00887>.
- Rutgersson, A., A.-S. Smedman, and U. Högström, 2001: Use of conventional stability parameters during swell. *J. Geophys. Res.*, **106**, 27 117–27 134, <https://doi.org/10.1029/2000JC000543>.
- Shearman, R. K., and S. J. Lentz, 2010: Long-term sea surface temperature variability along the U.S. East Coast. *J. Phys. Oceanogr.*, **40**, 1004–1017, <https://doi.org/10.1175/2009JPO4300.1>.
- Sirkova, I., 2012: Review on PE method application to propagation channel modeling in sea environment. *Cent. Eur. J. Eng.*, **2**, 19–38, <https://doi.org/10.2478/s13531-011-0049-y>.
- Small, R. J., and Coauthors, 2008: Air-sea interaction over ocean fronts and eddies. *Dyn. Atmos. Oceans*, **45**, 274–319, <https://doi.org/10.1016/j.dynatmoce.2008.01.001>.
- Smedman, A.-S., U. Högström, J. Hunt, and E. Sahlée, 2007: Heat/mass transfer in the slightly unstable atmospheric surface layer. *Quart. J. Roy. Meteor. Soc.*, **133**, 37–51, <https://doi.org/10.1002/qj.7>.
- Stapleton, J., D. Shanklin, V. Wiss, T. Nguyen, and E. Burgess, 2001: Radar propagation modeling assessment using measured refractivity and directly sensed propagation ground truth. NSWCCD Tech. Rep. NSWCCD/TR-01/132, 49 pp.
- Sullivan, P. P., J. B. Edson, T. Hristov, and J. C. McWilliams, 2008: Large-eddy simulations and observations of atmospheric marine boundary layers above nonequilibrium surface waves. *J. Atmos. Sci.*, **65**, 1225–1245, <https://doi.org/10.1175/2007JAS2427.1>.
- Sweet, W., R. Fett, J. Kerling, and P. La Violette, 1981: Air-sea interaction effects in the lower troposphere across the north wall of the Gulf Stream. *Mon. Wea. Rev.*, **109**, 1042–1052, [https://doi.org/10.1175/1520-0493\(1981\)109<1042:ASIEIT>2.0.CO;2](https://doi.org/10.1175/1520-0493(1981)109<1042:ASIEIT>2.0.CO;2).
- Tatarski, V. I., 1961: *Wave Propagation in a Turbulent Medium*. McGraw-Hill, 285 pp.
- Thompson, W., and T. Haack, 2011: An investigation of sea surface temperature influence on microwave refractivity: The Wallops-2000 Experiment. *J. Appl. Meteor. Climatol.*, **50**, 2319–2337, <https://doi.org/10.1175/JAMC-D-10-05002.1>.
- Turton, J. D., D. A. Bennetts, and S. F. G. Farmer, 1988: An introduction to radio ducting. *Meteor. Mag.*, **117**, 245–254.
- Xie, S., D. Yang, Y. Liu, and L. Shen, 2016: Simulation-based of wind loads on semi-submerged object in ocean wave field. *Phys. Fluids*, **28**, 015106, <https://doi.org/10.1063/1.4939271>.
- Yang, D., C. Meneveau, and L. Shen, 2013: Dynamic modeling of sea-surface roughness for large-eddy simulation of wind over ocean wave field. *J. Fluid Mech.*, **726**, 62–99, <https://doi.org/10.1017/jfm.2013.215>.

AMS BOOKS

RESEARCH APPLICATIONS HISTORY

AMS MEMBERS GET FREE

CLIMATE

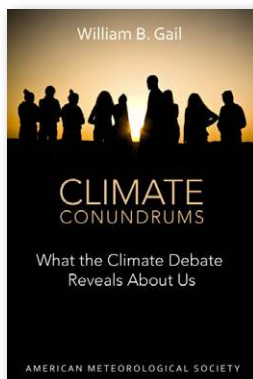
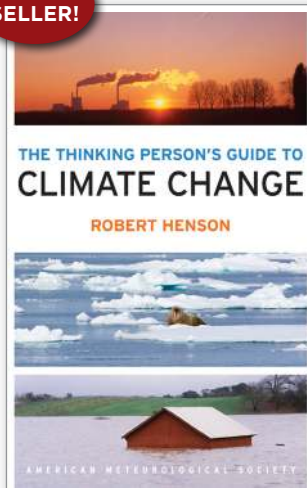
The Thinking Person's Guide to Climate Change

ROBERT HENSON

This fully updated and expanded revision of *The Rough Guide to Climate Change* combines years of data with recent research. It is the most comprehensive overview of climate science, acknowledging controversies but standing strong in its stance that the climate is changing—and something needs to be done.

© 2014, PAPERBACK, 520 PAGES,
ISBN: 978-1-935704-73-7
LIST \$30 MEMBER \$20

BEST
SELLER!

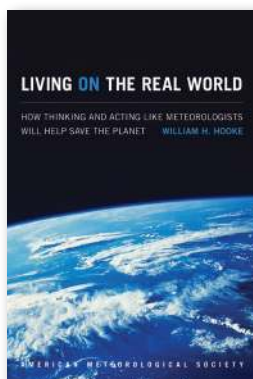


Climate Conundrums: What the Climate Debate Reveals about Us

WILLIAM B. GAIL

This is a journey through how we think, individually and collectively, about humanity's relationship with nature, and more. Can we make nature better? Could science and religion reconcile? Gail's insights on such issues help us better understand who we are and find a way forward.

© 2014, PAPERBACK, 240 PAGES,
ISBN: 978-1-935704-74-4 LIST \$30 MEMBER \$20



Living on the Real World: How Thinking and Acting Like Meteorologists Will Help Save the Planet

WILLIAM H. HOOKE

Meteorologists focus on small bits of information while using frequent collaboration to make decisions. With climate change a reality, William H. Hooke suggests we look to the way meteorologists operate as a model for how we can solve the 21st century's most urgent environmental problems.

© 2014, PAPERBACK, 272 PAGES, ISBN 978-1-935704-56-0 LIST \$30 MEMBER \$22

Synoptic-Dynamic Meteorology Lab Manual:

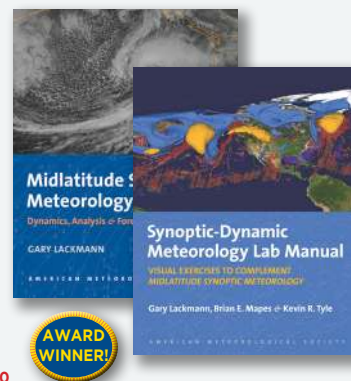
Visual Exercises to Complement Midlatitude Synoptic Meteorology

GARY LACKMANN,
BRIAN E. MAPES, AND
KEVIN R. TYLE

These labs link theoretical concepts with ground-breaking visualization to elucidate concepts taught in the award-winning companion textbook by Gary Lackmann, *Midlatitude Synoptic Meteorology*.

© 2017, PAPERBACK, 126 PAGES,
ISBN 978-1-878220-26-4

LIST \$80 MEMBER \$60 STUDENT \$50

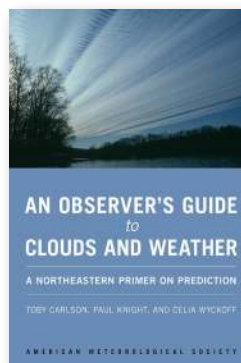


GUIDES

An Observer's Guide to Clouds and Weather:

A Northeastern Primer on Prediction

TOBY CARLSON, PAUL KNIGHT,
AND CELIA WYCKOFF



With help from Penn State experts, start at the beginning and go deep. This primer, intended for both serious enthusiasts and new meteorology students, will leave you with both refined observation skills and an understanding of the complex science behind the weather: the ingredients for making reliable predictions of your own. It connects fundamental meteorological concepts with the processes that shape weather patterns, and will make an expert of any dedicated reader.

© 2014, PAPERBACK, 210 PAGES,
ISBN: 978-1-935704-58-4 LIST \$30 MEMBER \$20

Eloquent Science: A Practical Guide to Becoming a Better Writer, Speaker, and Atmospheric Scientist

DAVID M. SCHULTZ

The ultimate communications manual for undergraduate and graduate students as well as researchers in the atmospheric sciences and their intersecting disciplines.

© 2009, PAPERBACK, 440 PAGES,
ISBN 978-1-878220-91-2

LIST \$45 MEMBER \$30



To order: bookstore.ametsoc.org, 617-226-3998, or use the order form in this magazine

NEW

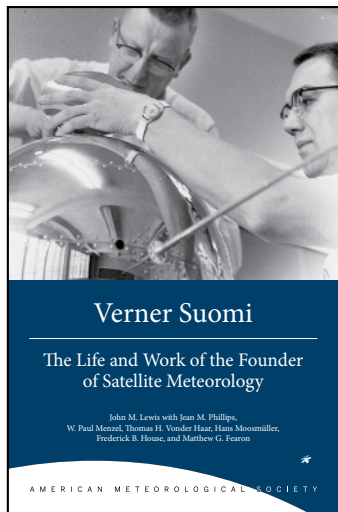
Verner Suomi: The Life and Work of the Founder of Satellite Meteorology

JOHN M. LEWIS WITH
JEAN M. PHILLIPS, W. PAUL
MENZEL, THOMAS H. VONDER
HAAR, HANS MOOSMÜLLER,
FREDERICK B. HOUSE,
AND MATTHEW G. FEARON

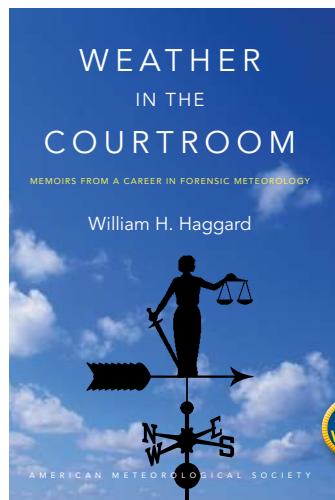
Born in a Minnesotan mining town, Suomi would spend his best years next door in Wisconsin, but not before seeing the whole world—from space, that is. This is the story of the scientist, inventor, and teacher who founded satellite meteorology, written by members of the communities that grew up around his groundbreaking work.

LIST \$30 MEMBER \$20

© 2016, PAPERBACK, 240 PAGES, ISBN: 978-1-944970-22-2



Weather in the Courtroom: Memoirs from a Career iForensic Meteorology



WILLIAM H. HAGGARD

From a pioneering forensic meteorologist, the inside scoop on legendary litigations, including the disappearance of an Alaskan congressman's airplane in 1972, the collapse of Tampa Bay's Skyway Bridge in 1980, and the crash of Delta Flight 191 in Dallas/Fort Worth in 1985.

LIST \$30 MEMBER \$20

© 2016, PAPERBACK, 240 PAGES,
ISBN: 978-1-940033-95-2



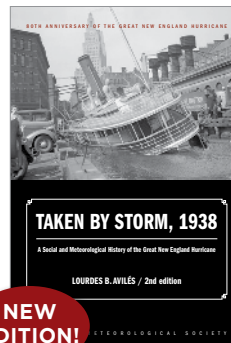
Booksellers, groups, or for examination copies:

The University of Chicago Press:
1-800-621-2736 (US & Canada)
773-702-7000 (all others)
custserv@press.uchicago.edu



AMS
American Meteorological Society

HISTORY



Taken by Storm, 1938:

A Social and Meteorological History of the Great New England Hurricane, 2nd Ed.

LOURDES B. AVILÉS

80TH
ANNIVERSARY
OF STORM

The science behind the 1938 Hurricane, which hit New England unannounced, is presented here for the first time along with new data that

sheds light on the motivations of the Weather Bureau forecasters. This compelling history successfully weaves science, historical accounts, and social analyses to create a comprehensive picture of the most powerful and devastating hurricane to hit New England to date.

© 2018, PAPERBACK, 288 PAGES, ISBN: 978-1-944970-24-6

LIST \$30 MEMBER \$20

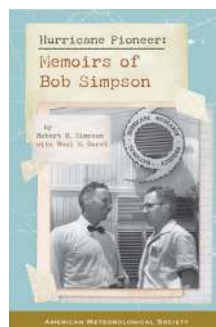
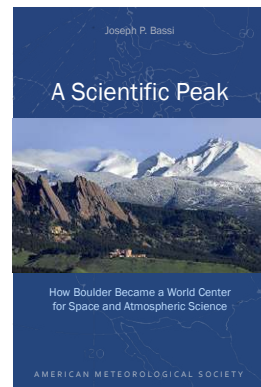
A Scientific Peak: How Boulder Became a World Center for Space and Atmospheric Science

JOSEPH P. BASSI

How did big science come to Boulder, Colorado? Joe Bassi introduces us to the characters, including Harvard sun-Earth researcher Walter Orr Roberts, and the unexpected brew of politics, passion, and sheer luck that during the Cold War era transformed this "Scientific Siberia" to home of NCAR and NOAA.

© 2015, PAPERBACK, 264 PAGES, ISBN: 978-1-935704-85-0

LIST PRICE: \$35.00 MEMBER PRICE: \$25.00



Hurricane Pioneer: Memoirs of Bob Simpson

ROBERT H. SIMPSON AND NEAL DORST

In 1951, Bob Simpson rode a plane into a hurricane—just one of the many pioneering exploits you'll find in these memoirs. Bob and his wife Joanne are meteorological icons: Bob was the first director of the National Hurricane Research Project and a director of the National Hurricane Center. He helped to create the Saffir-Simpson Hurricane Scale; the

public knows well his Categories 1-5. Proceeds from this book help support the AMS's K. Vic Ooyama Scholarship Fund.

© 2015, PAPERBACK, 156 PAGES

ISBN: 978-1-935704-75-1

LIST \$25

MEMBER \$20

AMS | Community

American Meteorological Society



Introducing a new AMS member benefit: AMS Community.

AMS Community is our new online platform that will revolutionize the way you communicate, connect, and interact with your fellow Society members!

Don't let the conversation end at a conference! With the AMS Community, you can engage with your colleagues any time, from any location.

AMS Community is a secure and easy-to-use private online forum, where AMS members can:

- **Participate** in focused and dedicated discussions relevant to you.
- **Contribute** your unique knowledge and perspective to the conversation.
- **Learn** from others in your field: Ask questions. Troubleshoot problems. Find resolutions.
- **Access** and **share** useful and informative documents and files in the Resource Library.
- **Network** with colleagues using our comprehensive Member Directory.
- **Stay up-to-date** with the latest AMS news and events.
- **Earn** recognition for the contributions you make to the Community.

We can't wait to have you join the conversation!
Activate your account with your existing AMS credentials today at:

community.ametsoc.org

Questions? Please contact amscommunity@ametsoc.org.